2013 CEF Run – Phase 1

Data Analysis and Model Validation

A. S. Choi

April 2014

SRNL-STI-2013-00705

DISCLAIMER

Printed in the United States of America

Prepared for
U.S. Department of Energy

SRNL-STI-2013-00705
Revision 0

Keywords: DWPF, MOG Flammability, CEF, Phase 1, Nitric-Formic Acid Flowsheet

Retention: *Permanent*

2013 CEF Run – Phase 1

Data Analysis and Model Validation

A. S. Choi

April 2014

Prepared for the U.S. Department of Energy under contract number DE-AC09-08SR22470.

Savannah River National Laboratory™
OPERATED BY SAVANNAH RIVER NUCLEAR SOLUTIONS

REVIEWS AND APPROVALS

AUTHOR:

A. S. Choi, Process Technology Programs Date

TECHNICAL REVIEW:

F. G, Smith, Process Modeling & Comp Chem Date

APPROVAL:

D. H. McGuire, Manager Date
Process Technology Programs

S. L. Marra, Manager Date
Environmental & Chemical Process Technology Research Programs

E. J. Freed, Manager Date
DWPF/Saltstone Facility Engineering, SRR

ACKNOWLEDGEMENTS

Expert reviews and timely programmatic guidance provided by T. L. Fellinger and E. W. Holtzscheiter of Savannah River Remediation throughout the process of developing the scope and budget of the CEF project are greatly appreciated. The author also would like to recognize the immense contributions made by M. Stone (Project Lead), F. Johnson (CEF Lead), and the rest of the CEF Team members to the successful planning and execution of the CEF Phase 1 Run. The author also would like to point out that the dedication by J. Zamecnik in setting up the comprehensive off-gas sampling system and collecting and post-run processing of a large amount of off-gas data was central to the successful completion of this study.

EXECUTIVE SUMMARY

Phase 1 of the 2013 Cold cap Evaluation Furnace (CEF) test was completed on June 3, 2013 after a 5-day round-the-clock feeding and pouring operation. The main goal of the test was to characterize the CEF off-gas produced from a nitric-formic acid flowsheet feed and confirm whether the CEF platform is capable of producing scalable off-gas data necessary for the revision of the DWPF melter off-gas flammability model; the revised model will be used to define new safety controls on the key operating parameters for the nitric-glycolic acid flowsheet feeds including total organic carbon (TOC). Whether the CEF off-gas data were scalable for the purpose of predicting the potential flammability of the DWPF melter exhaust was determined by comparing the predicted H_2 and CO concentrations using the current DWPF melter off-gas flammability model to those measured during Phase 1; data were deemed scalable if the calculated fractional conversions of TOC-to-H_2 and TOC-to-CO at varying melter vapor space temperatures were found to trend and further bound the respective measured data with some margin of safety. Being scalable thus means that for a given feed chemistry the instantaneous flow rates of H_2 and CO in the DWPF melter exhaust can be estimated with some degree of conservatism by multiplying those of the respective gases from a pilot-scale melter by the feed rate ratio. This report documents the results of the Phase 1 data analysis and the necessary calculations performed to determine the scalability of the CEF off-gas data.

A total of six steady state runs were made during Phase 1 under non-bubbled conditions by varying the CEF vapor space temperature from near 700 to below 300°C, as measured in a thermowell (T_{tw}). At each steady state temperature, the off-gas composition was monitored continuously for two hours using MS, GC, and FTIR in order to track mainly H_2, CO, CO_2, NO_x, and organic gases such as CH_4. The standard deviation of the average vapor space temperature during each steady state ranged from 2 to 6°C; however, those of the measured off-gas data were much larger due to the inherent cold cap instabilities in the slurry-fed melters. In order to predict the off-gas composition at the sampling location downstream of the film cooler, the measured feed composition was charge-reconciled and input into the DWPF melter off-gas flammability model, which was then run under the conditions for each of the six Phase 1 steady states. In doing so, it was necessary to perform an overall heat/mass balance calculation from the melter to the Off-Gas Condensate Tank (OGCT) in order to estimate the rate of air inleakage as well as the true gas temperature in the CEF vapor space (T_{gas}) during each steady state by taking into account the effects of thermal radiation on the measured temperature (T_{tw}).

The results of Phase 1 data analysis and subsequent model runs showed that the predicted concentrations of H_2 and CO by the DWPF model correctly trended and further bounded the respective measured data in the CEF off-gas by over predicting the TOC-to-H_2 and TOC-to-CO conversion ratios by a factor of 2 to 5; an exception was the 7X over prediction of the latter at T_{gas} = 371°C but the impact of CO on the off-gas flammability potential is only minor compared to that of H_2. More importantly, the seemingly-excessive over prediction of the TOC-to-H_2 conversion by a factor of 4 or higher at T_{gas} < ~350°C was attributed to the conservative antifoam decomposition scheme added recently to the model and therefore is considered a modeling issue and not a design issue. At T_{gas} > ~350°C, the predicted TOC-to-H_2 conversions were closer to but still higher than the measured data by a factor of 2, which may be regarded as adequate from the safety margin standpoint.

The heat/mass balance calculations also showed that the correlation between T_{tw} and T_{gas} in the CEF vapor space was close to that of the ½ scale SGM, whose data were taken as directly applicable to the DWPF melter and thus used to set all the parameters of the original model. Based on these results of the CEF Phase 1 off-gas and thermal data analyses, it is concluded that: (1) The thermal characteristics of the CEF vapor space are prototypic thanks to its prototypic design; and (2) The CEF off-gas data are scalable in terms of predicting the flammability potential of the DWPF melter off-gas.

These results also show that the existing DWPF safety controls on the TOC and antifoam as a function of nitrate are conservative by the same order of magnitude shown by the Phase 1 data at T_{gas} < ~350°C, since they were set at T_{gas} = 294°C, which falls into the region of excessive conservatism for the current DWPF model in terms of predicting the TOC-to-H_2 conversion.

In order to remedy the overly-conservative antifoam decomposition scheme used in the current DWPF model, the data from two recent tests will be analyzed in detail in order to gain additional insights into the antifoam decomposition chemistry in the cold cap. The first test was run in a temperature-programmed furnace using both normal and spiked feeds with fresh antifoam under inert and slightly oxidizing vapor space conditions. Phase 2 of the CEF test was run with the baseline nitric-glycolic acid flowsheet feeds that contained the "processed antifoam" and those spiked with fresh antifoam in order to study the effects of antifoam concentration as well as processing history on its decomposition chemistry under actual melter conditions. The goal is to develop an improved antifoam decomposition model from the analysis of these test data and incorporate it into a new multistage cold cap model to be developed concurrently for the nitric-glycolic acid flowsheet feeds. These activities will be documented in the Phase 2 report.

Finally, it is recommended that some of the conservatism in the existing DWPF safety controls be removed by improving the existing measured-vs.-true gas temperature correlation used in the melter vapor space combustion calculations. The basis for this recommendation comes from the fact that the existing correlation was developed by linearly extrapolating the SGM data taken over a relatively narrow temperature range down to the safety basis minimum of 460°C, thereby under predicting the true gas temperature considerably, as documented in this report. Specifically, the task of improving the current temperature correlation will involve; (1) performing a similar heat/mass balance analysis used in this study on actual DWPF data, (2) validating the measured-vs.-true gas temperature correlation for the CEF developed in this study against the DWPF melter heat/mass balance results, and (3) making adjustments to the CEF correlation, if necessary, before incorporating it into the DWPF safety basis calculations. The steps described here can be completed with relatively minimum efforts.

TABLE OF CONTENTS

LIST OF TABLES

LIST OF FIGURES

LIST OF ABBREVIATIONS

CEF	Cold cap Evaluation Furnace
CPC	Chemical Processing Cell
DCS	Distributed Control System
DWPF	Defense Waste Processing Facility
FTIR	Fourier Transform Infrared Spectroscopy
GC	Gas Chromatography
IC	Ion Chromatography
ICP	Invariant Condensed Phase
ICP-MS	Inductively Coupled Plasma Mass Spectrometry
LFL	Lower Flammability Limit
MCU	Modular Caustic-side solvent extraction Unit
MFT	Melter Feed Tank
MS	Mass Spectrometry
NGS	Next Generation Solvent
MSDS	Material Safety Data Sheet
OGCT	Off-Gas Condensate Tank
PDMS	Polydimethylsiloxane
PEO	polyethylene oxide
PSCM	Pilot Scale Ceramic Melter
SB	Sludge Batch
SGM	Scale Glass Melter
SME	Sludge Mix Evaporator
SRAT	Sludge Receipt and Adjustment Tank
SRNL	Savannah River National Laboratory
SRR	Savannah River Remediation
SVOA	semi-volatile organics
TMS	trimethylsiloxy
TOC	total organic carbon
TSR	Technical Safety Requirements
VSL	Vitreous State Laboratory

1.0 Introduction

The Defense Waste Processing Facility (DWPF) at the Department of Energy's (DOE) Savannah River Site (SRS) will undergo a flowsheet change to replace formic acid with glycolic acid as the baseline reductant for the high-level waste (HLW) melter feed.[1] Nitric acid is used in conjunction with either formic or glycolic acid to neutralize the alkaline sludge from the Tank Farms. So, the existing flowsheet is referred to as the nitric-formic acid flowsheet, while the new flowsheet is referred to as the nitric-glycolic acid flowsheet. Prior to implementation, the nitric-glycolic acid flowsheet feed will be fed to a pilot melter to demonstrate its processability, characterize the off-gas, and establish the technical bases for the melter off-gas flammability safety assessment. The off-gas surge potential of the nitric-glycolic acid flowsheet feed in terms of both condensable and non-condensable flows also needs to be quantified during the test in order to define the baseline melter transient for the safety analysis. The melter off-gas flammability assessment performed earlier in support of the down-select process indicated that a significant fraction of the glycolic acid added might remain undissociated and volatilize upon entering the melter, ending up in the condensate recycle to the Tank Farms.[2] Hence, it is also of vital importance to analyze the off-gas condensate produced during the test for the presence of glycolate or other organic species that may pose operational difficulties on the downstream processes.

The melter platform selected for the nitric-glycolic acid flowsheet demonstration is the Cold-cap Evaluation Furnace (CEF). The CEF is a $1/11^{th}$ scale DWPF melter based on the effective melt surface area, excluding those areas occupied by various penetrations.[3] It was used in 2010 to study the impact of glass bubblers on melter off-gas surging,[4] and the frequency and intensity of the off-gas surges during bubbled and non-bubbled CEF operations were found to be prototypic of the DWPF melter pressure spike data collected during 6 months before and 6 months after the bubblers went into operation.[5]

However, it is yet to be verified whether the CEF off-gas will exhibit the flammability potential that is also prototypic of the DWPF melter. Prototypic off-gas flammability potential means that the decomposition of non-volatile carbon species in the cold cap and subsequent combustion of calcine gases and volatile carbon species in the vapor space occur at similar rates in the two melters. Under such conditions, the resulting data will be scalable which in turn means that for a given feed chemistry the instantaneous flow rates of H_2 and CO in the DWPF melter off-gas can be estimated by multiplying those of the respective gases from a pilot-scale melter by the feed rate ratio. One way to confirm the scalability of the CEF data is to measure the concentrations of flammable gases in the CEF off-gas and compare them to those predicted by the DWPF melter off-gas flammability model, which was developed using the data taken during the ½ scale Scale Glass Melter (SGM) run with a nitric-formic acid flowsheet feed spiked with organic carbon species and validated against the data from two smaller melter runs.

For this reason, the alternate reductant demonstration melter test was divided into two phases. In Phase 1, the CEF was run with a nitric-formic acid flowsheet feed to confirm that measured concentrations of H_2 and CO in the CEF off-gas could be predicted and bounded by the current DWPF melter off-gas flammability model. Once the CEF is verified to be prototypic in terms of melter off-gas flammability potential, Phase 2 begins by feeding the CEF with the nitric-glycolic acid flowsheet feeds and collecting necessary data for the revision of the model for the alternate reductant flowsheet, including the new off-gas surge basis. The focus of this study was on the Phase 1 CEF run. Some of the key data collected and analyzed during Phase 1 and the results of subsequent model validation are documented in this report.

2.0 DWPF Melter Off-Gas Flammability Model

2.1 Original Model

The DWPF melter off-gas flammability model has been in use since the radioactive startup in 1996 to define the melter operating window for a given sludge batch in the form of Technical Safety Requirements (TSR) and feed interlocks.[6] It consists of two sub-models; the first model, called the 4-stage cold cap model, thermodynamically describes the chemistry of calcination and fusion reactions and calculates the compositions of two end products, calcine gases and glass, from a given feed composition. It was developed based on the ½ Scale Glass Melter 9th campaign (SGM-9) data and validated against the data from two smaller-scale melter runs.[7] The calculated composition of calcine gases is then used as the input to the second model, called the melter off-gas (MOG) dynamics model, which predicts the transient behavior of the DWPF MOG system under various upset scenarios.[8] Embedded in the MOG dynamics model is the vapor space combustion module that calculates the time-dependent concentrations of flammable gases in the melter exhaust using a global kinetics scheme to enable evaluation of the potential for off-gas flammability downstream. The baseline upset scenario for the MOG flammability safety analysis is an off-gas surge, which depends on the feed chemistry as well as the melter operating mode.[4]

2.2 Current Model

It is noted that the original cold cap model was developed and validated using the data produced with the nitric-formic acid flowsheet feeds that contained little antifoam and no free formic acid. The scope of the original model was expanded recently to account for the presence of significant levels of antifoam and free (undissociated) formic acid in the feed and their impact on the off-gas flammability. Specifically, the chemistry of antifoam decomposition was added to the cold cap model, while the chemistry of formic acid decomposition in the melter vapor space was added to the MOG dynamics model.

2.2.1 *Antifoam Decomposition*

Antifoam 747 is not a pure compound, as it is composed of low molecular weight trisiloxane polyether copolymers. The Material Safety Data Sheet (MSDS) lists it as a polyalkyleneoxide modified siloxane;[9] it is in essence a polyether chain capped with a trimethylsiloxane group at one end and a methoxy group at the other. Figure 2-1 shows the molecular structure of Antifoam 747 based on recent analytical results;[10] the polyethylene oxide (PEO) chain can have a varying number of ethylene oxide monomers (n), ranging from 7 to 9 in one group and 11 to 13 in the other.

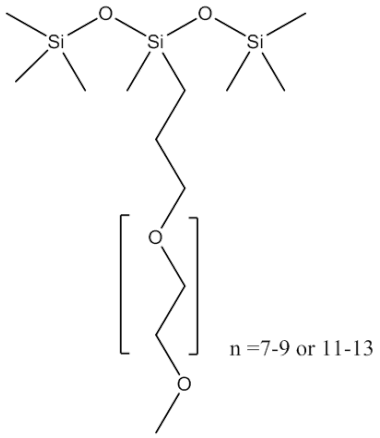

Figure 2-1. Molecular Structure of Antifoam 747 [from Ref. 10].

Assuming a 90:10 split between n=7-9 and n=11-13 groups, respectively, the average molecular weight of Antifoam 747 was calculated to be 664.65, and its elemental breakdown is shown in Table 2-1. It is noted that hydrogen accounts for less than 10% of pure antifoam by weight; however, due to its low molecular weight, it accounts for 60% on a molar basis and its H/C molar ratio of 2.3 is by far the highest of all the carbon sources in the DWPF melter feed.

Table 2-1. Elemental Makeup of Antifoam 747.

	(wt%)	(mole %)	(mole/mole of antifoam)
C	50.24	26.28	27.8
H	9.64	60.11	63.6
Si	12.68	2.84	3.00
O	27.44	10.78	11.4
Total	100.00	100.00	105.8

Two key assumptions were made in the current model regarding the fate of antifoam upon heat treatment in the Chemical Processing Cell (CPC) and melter:

1. The antifoam molecules do not undergo structural changes and/or degradation during the CPC processing, resulting in 100% retention in the melter feed.

2. The antifoam molecules completely break down in the melter as follows:

$$Antifoam + O_2 = SiO_2 + H_2 + CH_4 + CO + H_2O \quad (1)$$

It is noted that Eq. (1) is not written stoichiometrically balanced due to the varying lengths of the PEO chain. The products of antifoam decomposition are then allowed to undergo equilibrium reactions with other decomposition products of the remaining non-volatile feed components, before exiting the cold cap.

2.2.1.1 Assumption #1

There is ample experimental evidence that some fraction of the antifoam added is lost during the CPC processing, which makes the assumption of 100% retention of antifoam carbon in the melter feed conservative from the off-gas flammability standpoint. The first such evidence came during a series of bench-scale Sludge Receipt and Adjustment Tank (SRAT) runs in 2011; 68% of the recovered antifoam was found in the off-gas condensate, and the analysis using GC/MS revealed the presence of trimethylsilanol and its dimer hexamethyldisiloxane (HMDS), which suggests the cleavage of trimethylsiloxy (TMS) end groups.[11] However, since the recovery of antifoam added was low at <30%, the results could not be used to estimate the actual loss of antifoam during the SRAT processing.

In DWPF, an attempt was made to estimate the concentration of antifoam carbon remaining in each of the 15 SME batches (SME551-565) that were processed between Dec/2010 and Mar/2011 by subtracting the sum of formate and oxalate carbons (as measured by IC) from measured TOC. The results showed that on average approximately 20% of the fresh antifoam carbon added during the SRAT/SME processing was unaccounted for at the end of the SME cycle. Considering that the sum of all methyl carbons in the trisiloxane chain accounts for ~25% of the total carbon in the Antifoam 747 structure shown in Figure 2-1, the overall carbon balance around the DWPF CPC suggested that a significant fraction of methyl carbons indeed may have been detached from the trisiloxane chain and exited the slurry, while these batches underwent extended boil-up operation.

Recently, the off-gas data collected during Phase 1 CEF run showed that the concentration of CH_4 remained low at <20 ppm during non-bubbled low-temperature steady state runs and occasionally spiked to as high as 60 ppm under bubbled conditions. The most likely source for CH_4 is the methyl groups in Antifoam 747 due to the low dissociation energy of the Si-C bond (78 kcal/mole) compared to the other bonds present such as C-C (83 kcal/mole), C-O (86 kcal/mole), and Si-O (101-118 kcal/mole), which suggests that there should have been some leftover methyl groups in the feed. Table 2-2 lists the dissociation energies of selected carbon and silicon bonds. It is noted that the Phase 1 CEF feed was the SB6 simulant that went through a short SRAT cycle compared to DWPF and no SME cycle so the total duration during which the antifoam was exposed to the actual processing conditions was much shorter than those of SME551-565. However, no attempt has been made yet to estimate the cumulative evolution of CH_4 in order to see what fraction of the total methyl groups in the fresh antifoam it would be equivalent to.

These results indicate that the TMS group of Antifoam 747 could be cleaved from the PEO chain with relative ease compared to other bonds in the antifoam structure. However, the extent of such cleavage and subsequent loss of the degradation products is not known at this time in a sufficient enough detail to be used in the safety basis assessment. The assumption that 100% of antifoam added is retained in the melter feed is conservative from the off-gas flammability standpoint by as much as ~20%, as shown by the carbon balance of 15 full-scale SME batches.

Table 2-2. Bond Dissociation Energies of Selected Silicon and Carbon Bonds [Data taken from Ref. 12]

Bond	Energy, kcal/mole	Bond	Energy, kcal/mole
Si-Si	53	C-C	83
Si-C	78	C_{Ar}^{*}-C	98
Si-O	101-118	C-O	86
Si-H	75	C_{Ar}-O	107
Si-N	85	C-H	99
Si-F	135	C-N	73
Si-Cl	91	C_{Ar}-N	110
Si-Br	74	C-F	116
Si-I	56	C-Cl	81
		C-Br	68
		C-I	51

* C_{AR} represents aromatic carbon vs. C for non-aromatic carbon.

2.2.1.2 Assumption #2

As shown in Eq. (1), Assumption #2 allows Antifoam 747 to completely break down in the melter into the simple molecules of H_2, CH_4, CO, H_2O, and SiO_2. These decomposition products are then input into the cold cap model for further reaction with the decomposition products of other non-volatile feed components such as formate and nitrate salts. Therefore, the final composition of the antifoam degradation gases exiting the cold cap will not be as flammable as shown in Eq. (1). It is also shown that the decomposition of antifoam is thermo-oxidative, thus contributing additional reducing potential to the cold cap chemistry.

The necessary data to validate the adequacy of Assumption #2 were generated during a recent test in which a small batch of pure Antifoam 747 was heated under inert atmosphere using argon as a carrier gas in a furnace whose temperature was ramped from ambient to 1,150°C at 20°C/min.[13]

Shown in Figure 2-2 are the concentration profiles of the major gas species detected using Fourier Transform Infrared Spectroscopy (FTIR) and Mass Spectrometry (MS). Ignoring the inherent delay in the sample temperature caused by the heat transfer resistance, methane is shown to be the first gas species to evolve beginning at ~300°C, followed by ethylene and propylene at ~400°C, while acetylene did not begin to evolve until ~700°C. As discussed above, the likely source of CH_4 early on is the TMS group due to low dissociation energy of the Si-C bond. The evolution of the alkenes could be due to the cleavage of the PEO chain; it involves the cleavage of the C-O bond whose dissociation energy is higher than that of the Si-C bond, which explains their delayed appearance. Acetylene began to evolve just as the concentration of propylene began to decrease, and methane resumed increasing toward its peak, while the concentration of ethylene remained constant. All this appears to be well explained by the following disproportionation reaction:

$$C_3H_6 \rightarrow C_2H_2 + CH_4 \qquad (2)$$

It is also shown that while both H_2 and CO began to evolve at the same time at ~500°C, the concentration of H_2 did not begin to take off until the concentrations of the alkenes fell rapidly, which is a clear indication of pyrolysis, e.g.:

$$C_3H_6 \rightarrow CH_4 + H_2 + 2\,C \qquad (3)$$

$$C_2H_4 \rightarrow 2\,H_2 + 2\,C \qquad (4)$$

$$C + O^* \rightarrow CO \qquad (5)$$

where *O** represents the leftover oxygen radical after the pyrolysis of the polyether chain.

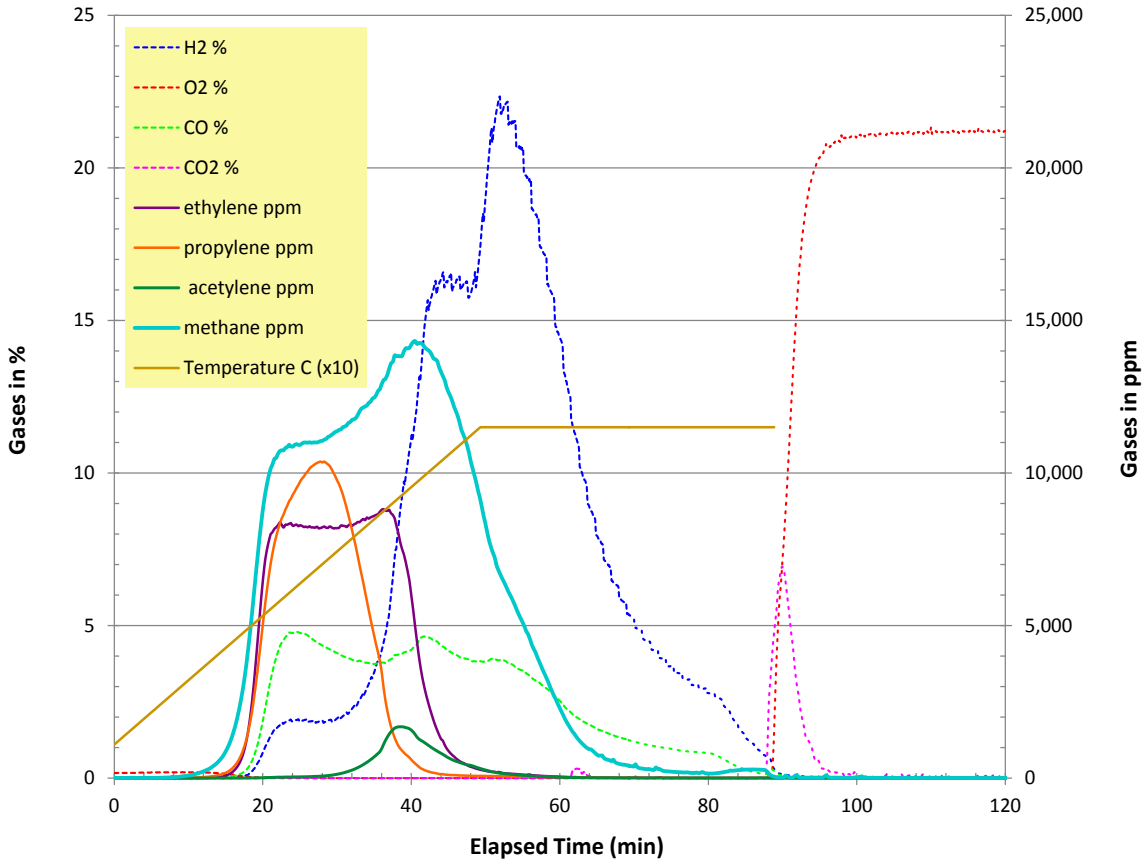

Figure 2-2. Off-Gas Profile during Pyrolysis of Antifoam 747.

As the furnace temperature approached 1,150°C, the alkenes and alkyne were no longer detected, and the concentration of CH_4 began to fall, which is again an indication of further pyrolysis into simpler molecules:

$$CH_4 \rightarrow C + 2\,H_2 \qquad (6)$$

As a result, the concentration of H_2 resumed climbing toward its peak, as shown in Figure 2-2, while CO remained more or less constant. The sample temperature at this point would have been considerably lower than the final target temperature of 1,150°C, since it will always lag behind the furnace control temperature due to the inherent heat transfer resistance, particularly for the transient temperature run employing a relatively high ramp rate like that used during this test. Thus it may be inferred that the actual thermal conditions of the sample at this point was close to those of the calcination regions of the cold cap model, i.e., Stages 1 and 2, whose temperatures range from 700 to 950°C. In addition, the gas species detected at this point such as H_2, CH_4, and CO are exactly the same as those assumed in the model, as shown in Eq. (1). Therefore, Assumption #2 appears to be in line with the data.

2.2.2 *Decomposition of Formic Acid*

The formic acid that remains undissociated at the end of a CPC cycle will volatilize upon entering the melter along with water and decompose in the vapor space via two parallel pathways:

$$\textit{Dehydration:} \qquad HCOOH \xrightarrow{k_1} CO + H_2O \qquad (7)$$

$$\textit{Decarboxylation:} \qquad HCOOH \xrightarrow{k_2} CO_2 + H_2 \qquad (8)$$

Obviously, assuming that formic acid decomposes exclusively via Eq. (8) would give the most H_2, thus conservative from the off-gas flammability standpoint. However, the gas-phase experiments have shown that the CO yield is substantially higher than that of CO_2, indicating that dehydration is the primary pathway, while the aqueous-phase experiments have shown decarboxylation as the primary pathway.[14] Furthermore, water is known to act as a homogeneous catalyst by lowering the activation energy barriers for both reaction pathways but decarboxylation is consistently more favorable than dehydration,[15] which means that although the dehydration pathway is favored in the gas-phase decomposition, the presence of water vapor in the melter vapor space by virtue of slurry feeding should promote the H_2 production via Eq. (8) to the extent yet to be determined.

Thus, two things must be known in order to assess the impact of formic acid on the melter off-gas flammability; (1) the overall rate of decomposition and (2) its partitioning between the dehydration and decarboxylation pathways. With no relevant data found in the literature from which to estimate the values of these two parameters, efforts were made earlier to see whether the general trends seen in the literature data taken under simple, controlled laboratory settings would also apply to the actual melter conditions,[2] and the basis for doing so was the data collected during the DM10 run in 2011.[16] One key assumption made was that formic acid vapor would not begin to decompose until T_{gas} > 163°C, which was the lowest vapor space gas temperature achieved during the DM10 runs. A partial support for this assumption comes from an earlier work, which showed that when formic acid vapor was passed through various glass tubes heated in a furnace, it did not decompose to any appreciable extent until T_{gas} = 250°C.[17] Since surface irregularities and impurities are known to increase the decomposition rate,[17,18] the potential for catalytic decomposition certainly existed in the DM10, and thus it is likely that formic acid began to decompose in the DM10 vapor space at a somewhat lower temperature than in the glass tubes.

The formic acid decomposition profile thus derived from the DM10 data showed that as expected the overall decomposition rate increased with increasing temperature; initially, it increased slowly that the overall conversion was still below 20% at T_{gas} = 300°C, above which it began to increase rapidly to 100% at $T_{gas} \geq$ 390°C.[2] Furthermore, it appeared that formic acid decomposed exclusively via the dehydration pathway (Eq. 7) at T_{gas} < 300°C, which agrees with the general trend seen in the literature data taken in the absence of water. Incidentally, the DM10 vapor space was actively purged with ambient air in an effort to lower T_{gas} below 300°C and, as a result, the partial pressure of water vapor was relatively low, ranging from 30 to 75 mmHg.

As the temperature was increased above 300°C, not only the rate of decomposition accelerated but the fraction of the formic acid decomposed via the dehydration pathway decreased sharply to the 0.5-0.6 range, which means that the decomposition product ratio CO/CO_2 decreased with increasing temperature according to Eq. (7) and (8). Since the CO/CO_2 ratio is equivalent to that of the corresponding rate constants, k_1/k_2, it can be said that the k_1/k_2 ratio also decreased with increasing temperature, which is in qualitative agreement with the trends seen in the shock-tube experiments, although the temperature range of the latter was much higher.[14]

Although insight was gained, the quantitative DM10 results were not incorporated directly into the DWPF model, since its design is not prototypic, while both the overall rate and pathway of the formic acid decomposition are expected to be sensitive to the melter design and operating conditions as much as the first-order global kinetics of the H_2 and CO oxidation are.[2] As a result, the decomposition behavior of formic acid vapor was modeled based on the qualitative trends seen in the literature data and further confirmed by the DM10 data; however, the quantitative DM10 results were modified somewhat in part to help smooth out some of the irregularities in the data, before incorporating them into the DWPF model.

Once formed, the decomposition products of Eq. (7) and (8) are assumed in the current DWPF model to exit the melter without undergoing further reactions due to the slow kinetics of the gas-phase decomposition of formic acid. In addition, since the volatilization of water and free formic acid is not truly instantaneous, it is expected that some fraction of the latter will decompose in the cold cap predominantly by Eq. (8). In that case, the resulting flammable decomposition products will get oxidized in the vapor space according to the first-order global kinetics. However, the aqueous-phase decomposition of formic acid in the cold cap is not included in the current model.

3.0 Phase 1 CEF Run

3.1 Overview

The Phase 1 CEF run began on May 30 and was completed on June 3, 2013, lasting for 5 days. The SB6 simulant used did not contain mercury or noble metals since they are not known to affect the melter off-gas flammability directly and thus are not part of the input vector for the DWPF model. However, their presence is known to strongly affect the oxidant (nitrate) and reductant (TOC) balances in the melter feed, which in turn affects the rheological properties as well as the cold cap chemistry in terms of redox and off-gas flammability. For this reason, a series of 4L SRAT runs were performed in order to provide the operating instructions for the nitric-formic acid addition and subsequent boil-up at an off-site vendor's facility (Harrell) so that the SRAT product would meet all the target properties set for the Phase 1 feed in the absence of mercury or noble metals.[19]

The resulting SRAT product received was blended with Frit 418 at 36% target waste loading just prior to being fed to the CEF. The measured redox of the feed averaged 0.26 in a sealed crucible. The CEF was run at 6 different vapor space temperature targets: 700, 600, 500, 400, 350, <300°C. Once steady state was established at each temperature, the off-gas composition was measured downstream of the film cooler for at least 2 hours using FTIR, GC, and MS. Details of the overall Phase 1 run, including the latest design changes made to the CEF, feed preparation, execution of steady state temperature runs, off-gas monitoring, and sampling are documented in a separate report.[20] This report documents some of the key Phase 1 data and subsequent analysis performed to determine whether the CEF is prototypic in terms of predicting the DWPF melter off-gas flammability.

3.2 Feed Composition

The analytical data for the as-received SRAT product are given in Table 3-1 and Table 3-2 for the slurry and supernate, respectively. It is noted that any supernate cation data below 10 mg/L were excluded from Table 3-2. At pH of 4.95, some fraction of the measured total formate of 60,100 mg/kg is expected to be in the form of undissociated free formic acid, whose concentration is calculated during the charge-reconciliation step described next.

Table 3-1. Analytical Data for the SRAT Product Made by Harrell (Slurry).

Elements:	wt% calcine solids	Anions:	mg/kg slurry
Al	13.939	F	<500
Ba	0.137	Cl	450
Ca	1.198	NO_2	<500
Cr	0.194	NO_3	24,250
Cu	0.118	SO_4	1,080
Fe	21.550	C_2O_4	<500
K	0.264	COOH	60,100
Mg	0.853	PO_4	<500
Mn	6.723		
Na	13.215	**Bulk Properties:**	
Ni	2.858	density	1.1494
P	0.102	pH	4.95
S	0.305	total solids	28.3%
Si	1.490	calcine solids	17.7%
Ti	0.054	insoluble solids	15.8%
Zn	0.107	soluble solids	12.5%
Zr	0.191		
total	63.299		

Table 3-2. Analytical Data for the SRAT Product Made by Harrell (Supernate).

Cation:	mg/L	Anion:	mg/L
Al	42	F	<500
Ca	2,725	Cl	593
Cu	58	NO_2	<500
K	1,045	NO_3	36,500
Mg	1,966	SO_4	2,130
Mn	9,077	C_2O_4	<500
Na	33,900	COOH	63,750
Ni	1,602	PO_4	<500
S	624		
Si	261	**Bulk Properties:**	
Zn	23	density	1.0972
total	51,322		

3.3 Charge Reconciliation

The charge imbalances present in the SRAT product slurry and supernate data given in Table 3-1 and Table 3-2, respectively, were reconciled simultaneously under the constraints of measured bulk properties, and the resulting composition of the charge-reconciled SRAT Product is given in Table 3-3 in a neutral species form. In order to achieve charge balance, the measured Na data by ICP-MS was adjusted up by 11%, while the equilibrium dissociation of HCOOH at the measured pH of 4.95 was adjusted down by 10% from the calculated value using its pK_a value of 3.75 at 25°C. The resulting insoluble and soluble solids are shown to be within 10% and 2% of measured data, respectively. The concentration of free formic acid thus calculated was 0.267 M, which is equivalent to 15.6% of the measured formate by IC. Both formic acid and water volatize upon entering the melter and thus constitute the only volatile components in the Phase 1 feed.

Since the presence of antifoam molecules cannot be detected directly by the analytical methods used, its concentration was set based on addition history, assuming 100% retention; Antifoam 747 was added at 3.013 kg per 900 kg of simulant or 0.1169 kg/kg Fe during the SRAT processing at Harrell. Furthermore, since soluble oxalate was below detection limit of IC in both the slurry and supernate samples, the concentration of insoluble oxalate was set to counterbalance the remaining insoluble Ca after satisfying the insoluble sulfate data as $CaSO_4$. The resulting insoluble oxalate shown as CaC_2O_4 in Table 3-3 represents 2% of the total oxalate added to the SB6 simulant as $Na_2C_2O_4$, which means that up to 98% of the oxalate added could have been destroyed during the SRAT processing. Although the analytical results indicated that practically all of the phosphate added to the simulant as $Na_3PO_4 \cdot 12H_2O$ at 0.021 g/g Fe remained insoluble, it was assumed to be 100% soluble in order to help achieve the charge balance. This adjustment, however, will have no impact on the outcome of this study other than the overall charge balance, since the concentration of phosphate is low and does not participate in the cold cap or vapor space combustion reactions to any appreciable extent to impact either the glass redox or off-gas flammability.

Table 3-3. Composition of Charge Reconciled CEF Phase 1 SRAT Product.

Insolubles	g/L	Solubles	g/L	Volatiles	g/L
$Fe(OH)_3$	85.4790	$Ca(COOH)_2$	5.8507	HCOOH	12.2657
$Al(OH)_3$	83.4191	$Ca(NO_3)_2$	2.6701	H_2O	796.4228
MnO_2	9.1149	$Al(COOH)_3$	0.1687	Total_3	808.6885
$Ni(OH)_2$	7.0783	$Al(NO_3)_3$	0.0803		
$Cr(OH)_3$	0.7961	$Cu(COOH)_2$	0.0927	Total Slurry	1,145.3500
$Cu(OH)_2$	0.2946	$Cu(NO_3)_2$	0.0410		
TiO_2	0.1859	KCOOH	0.8657		
SiO_2	6.1072	KNO_3	0.3766		
$Zn(OH)_2$	0.3062	$Mg(COOH)_2$	6.1045		
$BaSO_4$	0.4827	$Mg(NO_3)_2$	2.8655		
ZrO_2	0.5347	$Mn(COOH)_2$	15.8403		
$CaSO_4$	0.0679	$Mn(NO_3)_2$	7.0757		
CaC_2O_4	0.0280	NaCl	0.8526		
Antifoam	5.2218	NaCOOH	66.5075		
Total_1	199.1163	$NaNO_3$	23.8583		
Measured	181.0717	Na_3PO_4	1.1215		
Δ (%)	9.9654	$Ni(COOH)_2$	2.6845		
		$Ni(NO_3)_2$	1.1934		
		$Zn(COOH)_2$	0.0364		
		$Zn(NO_3)_2$	0.0161		
		Na_2SO_4	2.4403		
		H_4SiO_4	0.8029		
		Total_2	141.5452		
		Measured	143.7000		
		Δ (%)	-1.4995		
		Total Solids	340.6615		
		Measured	324.7717		
		Δ (%)	4.8926		

The SRAT product composition shown in Table 3-3 was blended next with Frit 418 at the target waste loading of 36% and adjusted to 42 wt% total solids. The resulting composition of the Phase 1 CEF feed is shown in Table 3-4; the composition is given in terms of instantaneous mass flow rates required to satisfy the DWPF design basis glass production rate of 228 lb/hr. The feed included 16,682 ppm nitrate and 46,100 ppm formate; the latter accounted for 76% of the 13,869 ppm TOC, whose distribution is shown in Table 3-5.

Although antifoam carbon is shown to account for only 11% of the TOC, its impact on the off-gas flammability will be much greater since its H/C ratio is 2.3X that of the formate carbon. It is also noted that the resulting TOC including the calculated antifoam content of 1,571 ppm assuming 100% retention was still 3.3% below the average of the measured data by the DWPF Analytical Lab that ranged from 13,872 to 15,381 ppm. Nevertheless, the excellent agreement between the measured and calculated TOC suggests that no appreciable degradation of antifoam occurred during the SRAT processing at Harrell contrary to what previous bench- and full-scale data showed also without the presence of noble metals. However, it is still unknown whether antifoam degradation would accelerate in the presence of noble metals.

Table 3-4. Phase 1 CEF Feed Rate at 228 lb/hr Glass Production.

Insolubles	lb/hr	Solubles	lb/hr	Volatiles	lb/hr
$Fe(OH)_3$	34.5460	$Ca(COOH)_2$	2.3645	HCOOH	4.9571
$Al(OH)_3$	33.7135	$Ca(NO_3)_2$	1.0791	H_2O	386.6766
MnO_2	3.6838	$Al(COOH)_3$	0.0682	Total_3	391.6337
$Ni(OH)_2$	2.8607	$Al(NO_3)_3$	0.0324		
$Cr(OH)_3$	0.3218	$Cu(COOH)_2$	0.0375	Total Slurry	675.2305
$Cu(OH)_2$	0.1191	$Cu(NO_3)_2$	0.0166		
TiO_2	0.0751	KCOOH	0.3499		
SiO_2	113.3674	KNO_3	0.1522		
Na_2O	11.6736	$Mg(COOH)_2$	2.4671		
$Zn(OH)_2$	0.1237	$Mg(NO_3)_2$	1.1581		
B_2O_3	11.6736	$Mn(COOH)_2$	6.4018		
Li_2O	11.6736	$Mn(NO_3)_2$	2.8596		
$BaSO_4$	0.1951	NaCl	0.3446		
ZrO_2	0.2161	NaCOOH	26.8787		
$CaSO_4$	0.0274	$NaNO_3$	9.6422		
CaC_2O_4	0.0113	Na_3PO_4	0.4532		
antifoam	2.1104	$Ni(COOH)_2$	1.0849		
Total_1	226.3920	$Ni(NO_3)_2$	0.4823		
		$Zn(COOH)_2$	0.0147		
		$Zn(NO_3)_2$	0.0065		
		Na_2SO_4	0.9862		
		H_4SiO_4	0.3245		
		Total_2	57.2048		

Table 3-5. TOC Distribution of Phase 1 CEF Feed.

Carbons	lb/hr	ppm	(%)	H/C
Formate	7.0113	10,383	74.8	1.0
Oxalate	0.0021	3	<0.1	0.0
Free Formic	1.2936	1,916	13.8	2.0
Antifoam	1.0608	1,571	11.3	2.3
TOC	9.3678	13,874	100.0	
measured TOC		14,352		
Δ TOC		-3.3%		

3.4 Steady State Phase 1 Data

Some of the key CEF operating data taken during the six steady state runs are given in Table 3-6 along with the concentrations of the major off-gas species detected. The actual steady state vapor space (VS) temperatures were all within ±10°C of the target temperatures. It can be seen that the VS temperatures of 500°C and lower were achieved in part by additional air purge to the CEF vapor space beyond the nominal 10 scfm. However, since the blower could not handle increased air flows at these lower temperatures as well as it was expected to, the film cooler air flow had to be reduced in order to keep the melter pressure under vacuum. As expected, the steady state feed rates decreased with decreasing vapor space temperature. However, the rate of decrease in feed rate was not quite uniform; there was a sharp drop-off in steady state feed rate from 507 to 409°C.

Despite the fact that the melt pool was not agitated with the glass bubblers throughout the steady state runs, the upper and lower melt temperatures remained within ±10°C of each other except at T_{vs} = 693 and 507°C, where the upper melt temperatures were 40 to 50°C lower than the lower melt temperatures. Across all six steady state runs, the average melt pool temperatures fluctuated by ±5°C. As stated above, the entire data collected during the Phase 1 runs, both non-bubbled and bubbled, including the melter turnover are documented elsewhere,[19] and only the data relevant to the off-gas flammability analysis are presented later in this report.

Table 3-6. Key CEF Operating Variables and Off-Gas Data for Six Steady State Runs.

VS Temp (°C)	Feed Rate (g/min)	Melt Temp (°C)	CEF Press ("H_2O)	CEF Air (scfm)	FC Air (scfm)	OG Temp (°C)	H_2 (GC) (ppm)	CO (FTIR) (ppm)	CO_2 (MS) (vol%)
693	89.0	1072	-5.04	9.8	14.6	325	32	81	0.35
596	83.6	1071	-5.23	9.8	14.8	272	117	91	0.34
507	82.4	1061	-4.74	17.4	15.0	258	95	38	0.23
409	59.2	1063	-3.50	28.1	7.8	253	71	26	0.17
346	54.8	1071	-3.14	33.0	5.6	235	74	29	0.17
287	53.7	1066	-0.50	38.9	5.6	210	64	21	0.15

Except for CH_4 which was detected at <10 ppm, the only flammable gases identified during Phase 1 were H_2 and CO, and it was the purpose of this study to confirm whether the existing DWPF melter off-gas flammability model could predict the H_2 and CO concentrations given in Table 3-6 under the same melter off-gas operating conditions used to generate such data. Before doing so, however, two unknowns that directly impact the vapor space combustion calculations must be estimated from the data collected. The first unknown is the rate of air inleakage into the CEF vapor space, which then enables the total air available for both combustion and dilution to be known accurately. The second is the actual gas temperature in the CEF vapor space at each measured temperature, since it is the former that is used in the vapor space combustion kinetics calculations. Since gases are mostly transparent to infrared radiation, the actual gas temperatures tend to be lower than measured temperatures using thermocouples, and the magnitude of difference between the two temperatures depends on both the design of melter cavity and a host of operating variables, including the feed rate and temperature itself. Furthermore, since those two unknowns are interdependent, they were solved simultaneously by performing an overall energy balance around the film cooler, assuming that the CEF vapor space is well-mixed reactor.

4.0 Model Validation

Since only the steady state conditions were considered in this study, it was not necessary to run the system dynamics portion of the MOG dynamics model. Instead, a spreadsheet was developed that calculates the steady state component mass and energy balances from the melter to the off-gas condensate tank (OGCT). The output of the cold cap model was input into this spreadsheet, which was used to estimate both air inleakage and actual gas temperature iteratively and further calculate the global kinetics of H_2 and CO combustion in the CEF vapor space. The steps that were followed to validate the existing DWPF melter off-gas flammability model included: (1) development of the input vector for the 4-stage cold cap model, (2) execution of the 4-stage cold cap model and post-processing of the output to develop the input vector for the spreadsheet, (3) steady state component mass and energy balance calculations from the melter to the OGCT and validation of the DWPF model, and (4) further analysis of the Phase 1 data in light of the model validation results.

4.1 Cold Cap Model Run

4.1.1 *Model Input*

The Phase 1 feed composition given in Table 3-4 was converted into the 4-stage cold cap model input using the following bases and assumptions:[6]

1. All salts except sulfates were pre-decomposed into oxides and gases:

   Stage 1: $2\ NaCOOH = Na_2C_2O_4 + H_2$ (9)
   $2\ NaNO_3 = 2\ NaNO_2 + O_2$ (10)
   $2\ Fe(OH)_3 = Fe_2O_3 + 3\ H_2O$ (11)

   Stage 2: $Na_2C_2O_4 = Na_2O + CO + CO_2$ (12)
   $2\ NaNO_2 = Na_2O + NO + NO_2$ (13)

2. Those species involving Ba, Cl, Cr, P, Ti, Zn, and Zr were excluded from the model input, since they either were present at trace-level concentrations and/or have little or no impact on the glass redox or off-gas flammability. For the Phase 1 CEF feed, the species thus omitted from the input made up for only 0.41 wt% of the dried feed solids including free formic acid.

3. The decomposition products of nitrate salts via Eq. (10) and (13) were fed to Stages 1, 2 and 3 at the 30:50:20 ratios, respectively.

4. 100% of the decomposition products of Antifoam 747 via Eq. (1) were fed to Stage 1.

5. Volatile species such as H_2O and HCOOH were excluded from the model input; instead, they were fed directly to the vapor space reactor along with the calcine gases.

6. The instantaneous flow rate of each feed constituent was set at the DWPF design basis glass production rate of 228 lb/hr.

The resulting input vector for the 4-stage cold cap model run is shown in Table 4-1. The given distribution of oxides and gases among various cold cap stages is based on available literature data on the calcination and fusion of non-volatile feed solids. For instance, the decomposition of sodium formate into sodium oxalate and H_2 (Eq. 9) is essentially complete at just above 400°C;[21] therefore, all of the H_2 released during the decomposition of formate salts was fed to Stage 1, whose equilibrium temperature is set at 700°C. The subsequent decomposition of sodium oxalate occurs in two stages;[22] it first converts to sodium carbonate by releasing CO with the conversion being complete between 750 and 800°C, while the sodium carbonate begins to decompose at above 810°C into Na_2O and CO_2. Since the equilibrium temperature of Stage 2 is set at 900°C, the decomposition reactions of oxalate salts into oxides and CO/CO_2 are combined into one reaction (Eq. 12), and their decomposition products are fed to Stage 2.

There exists ample experimental evidence that the primary step in nitrate decomposition is the formation of nitrite and O_2 (Eq. 10), and the subsequent decomposition of nitrite can take several different routes, depending on the presence or absence of air.[23] Since the cold cap cannot be considered an inert environment, and the decomposition of nitrate continues above 900°C, it was assumed that nitrate salts would decompose via the combined reactions of Eq. (10) and (13) throughout Stages 1, 2 and 3 at the 30:50:20 ratios, respectively.[6]

Table 4-1. Input to 4-Stage Cold Cap Model at 228 lb/hr Glass Production Rate.

Species	Stage 1 (gmole/hr)	Stage 2 (gmole/hr)	Stage 3 (gmole/hr)
Al_2O_3	0	98.0241	0
B_2O_3	76.0576	0	0
CaO		11.2664	0
CuO	0.7042	0	0
Fe_2O_3	73.3143	0	0
K_2O	1.28478	0	0
Li_2O	0	177.2054	0
MgO	0	0	13.3290
MnO_2	0	19.2203	0
MnO	27.2788	0	0
Na_2O	115.3678	87.3155	0
NiO	18.5028	0	0
SiO_2	861.7071	0	0
$CaSO_4$	0	0	0.0914
Na_2SO_4	0	0	3.1495
H_2O	538.6390	0	0
CO	25.7926	132.4314	0
CO_2	0	132.4314	0
H_2	145.3536	0	0
O_2	0.8382	20.6003	8.2401
NO	12.3602	20.6003	8.2401
NO_2	12.3602	20.6003	8.2401
Volatiles to the Vapor Space			
HCOOH	48.8545		
CH_4	14.2706		

4.1.2 *Model Output*

The key features of the original 4-stage cold cap model including the software and its free energy database are given elsewhere.[7] The current model with the antifoam decomposition stoichiometry per Eq. (1) was run with the input vector shown in Table 4-1, and the calculated compositions (or flow rates) of glass and calcine gases are shown in Table 4-2. It is seen that the predicted glass compositions are split in groups or phases; the letter *l* after each species in the melt phase denotes "liquid." These liquid or melt species do not necessarily represent independent molecular or ionic species but serve to represent the local associative order.[24] Due to structural similarities, spinels readily form solid solutions with one another and thus are allowed to form a separate phase of their own. On the other hand, each of the species included in the Invariant Condensed Phase (ICP) is assumed to form a separate phase by itself. Hence, as more species are included in the ICP, the total number of phases to be considered in the equilibrium calculations increases proportionally, thus making it more difficult to achieve convergence.

Table 4-2. 4-Stage Cold Cap Model Output for Phase 1 CEF Feed.

Melt Phase	(gmole/hr)	Calcine Gases	(gmole/hr)
SiO_2 l	632.9400	H_2O	603.4040
Na_2SiO_3 l	205.8000	CO_2	274.1710
$LiBO_2$ l	151.3790	H_2	109.0780
$LiAlO_2$ l	196.0000	N_2	41.1973
Fe_3O_4 l	33.9296	CO	30.7837
$MgSiO_3$ l	12.8572	SO_2	0.0038
FeO l	20.8174	$NaBO_2$ g	0.0002
$CaFe_2O_4$ l	1.4137	NH_3	0.0055
B_2O_3 l	0.0008	CH_4	0.0049
Ca_2SiO_4 l	2.6929	Total	1058.6484
$Ca_3MgSi_2O_8$ l	0.4416		
Fe_2SiO_4 l	5.6014	CO/CO_2 =	0.1123
Li_2O l	3.5104	$H_2/(CO+CO_2)$ =	0.3577
K_2SiO_3 l	0.9255		
KBO_2 l	0.7190		
Spinel Phase			
$NiFe_2O_4$	4.2466		
Mn_3O_4	15.0947		
$CuFe_2O_4$	0.7040		
$MgFe_2O_4$	0.0312		
ICP			
Fe_2O_3	0		
NiO	14.2534		
$CaSO_4$	3.2372		
MnO	1.2158		
Redox			
Calculated Fe^{+2}/Fe^{total} =		0.45	
Measured in sealed crucible =		0.26	

The CEF Phase 1 feed contained 16,682 ppm nitrate and 13,874 ppm TOC for a TOC/nitrate ratio of 0.83; the ratio is used here as a relative measure of the oxidizing or reducing power of feed. At this high TOC/nitrate ratio and the TOC distribution given in Table 3-5, the calculated redox of the CEF Phase 1 glass was 0.45 compared to the measured average of 0.26 in a sealed crucible; the model thus over predicted redox by a wide margin. Since the 4-stage cold cap model was updated by adding the antifoam decomposition scheme shown in Eq. (1), its adequacy was tested earlier against the data from the SB8 simulant CPC study;[25] the predicted redox of SB8-D3 glass was 0.11 compared to the sealed crucible data that ranged from 0.17 to 0.23.[6] These results show that the model predicted the observed trend of increasing redox with increasing TOC/nitrate ratio correctly but the predicted slope of increase was too stiff.

To help find the potential causes for the high model sensitivity, the nitrate and TOC distributions of the two feeds are compared in Table 4-3. It is seen that the pH of the SB8-D3 SME product was slightly above neutral so it contained no free formic acid unlike the acidic CEF Phase 1 feed. However, since formic acid will not impact redox thanks to its volatility, it can be excluded from further consideration. Then, the large increase in the predicted redox of the CEF Phase 1 glass should be attributed mainly to the differences in the formate, antifoam, and nitrate levels in the

two feeds. Furthermore, considering the fact that the original cold cap model was validated for three different formic acid flowsheet feeds that contained varying amounts of formate and nitrate but little or no antifoam,[7] it may be postulated that the assumed antifoam decomposition scheme and/or subsequent equilibrium reactions of the decomposition products with other non-volatile feed constituents set up under the current model construct is not accurate at ~4X higher antifoam carbon level of the CEF Phase 1 feed. Efforts are currently underway to address this deficiency by collecting data from on-going furnace tests and the Phase 2 CEF run using feeds containing both fresh and processed antifoam.

Table 4-3. Comparisons of SB8-D3 and CEF Phase 1 Feed Characteristics.

	SB8-D3	CEF Phase 1
pH	7.44	4.95
Formate (ppm)	14,512	10,383
Oxalate (ppm)	716	3
Free Formic (ppm)	0	1,916
Antifoam (ppm)	419	1,571
TOC (ppm)	15,658	13,874
TOC – Free Formic (ppm)	15,658	11,958
Nitrate (ppm)	28,980	16,682
TOC/Nitrate	0.54	0.83
TOC/Nitrate exc. Free Formic	0.54	0.72
Calculated Redox	0.11	0.45
Measured Redox	0.21	0.26

Under the current model construct, higher predicted redox than measured generally means that less O_2 was made available to the equilibrium reactions of the condensed phases, since the total inventory of O_2 is fixed for a given feed. This in turn means that the remaining O_2 not made available to the condensed-phase reactions was used instead to carry out the gas-phase reactions in the cold cap, including the oxidation of flammable gases. Therefore, if the inventory of O_2 in the CEF Phase 1 non-volatile feed were to be re-partitioned under the current model construct so as to match the measured redox by shifting more O_2 to the condensed phase, the resulting concentrations of H_2 and CO in the calcine gases would be higher than the predicted values shown in Table 4-2. The impact of this re-partitioning of O_2 on the overall conclusion of this study will be assessed later in this report. As a result, the molar ratios of $H_2/(CO+CO_2)$ and CO/CO_2 in the calcine gases would also be higher than shown. As with the TOC/nitrate ratio for redox, it was shown earlier that the molar ratio of $H_2/(CO+CO_2)$ can be used as an indicator of the relative flammability of calcine gases for a given feed.[6]

4.2 Mass and Energy Balance Calculations

A spreadsheet was used to perform the component mass and energy balance calculations from the CEF vapor space to the OGCT for the six steady state runs made during Phase 1. This section describes the input and output of the spreadsheet along with further interpretation of data in light of calculated results. The ultimate goal was to find out how close the calculated potential for off-gas flammability was to the measured data downstream of the film cooler, particularly H_2 and CO.

4.2.1 *Spreadsheet Input*

The input for the spreadsheet calculations included all the measured pressure, temperature, and flow data as well as the instantaneous flow rates of calcine gases calculated by the cold cap model, including volatiles. In order to simulate actual steady state conditions, the flow rates of calcine gases and volatiles shown in Table 4-2 were scaled down by the ratio of each steady state glass pour rate, which was calculated from the measured average feed rate, to that of the DWPF design basis. The CEF-to-DWPF glass pour rate ratios thus used are given in Table 4-4 along with the resulting instantaneous flow rates of calcine gases and volatiles. These adjusted process gas flows and the air purges constituted the input flows to the vapor space reactor, where flammable gases such as H_2 and CO were oxidized according to the global combustion kinetics developed earlier,[7] while the decomposition of formic acid vapor was modeled based in part on the DM10 results.

However, before such reaction kinetics could be calculated, the rate of air inleakage to the CEF vapor space at each measured vacuum and the true gas temperature at each measured CEF vapor space temperature needed to be determined first. This was accomplished by performing an overall mass and energy balance around the film cooler and, as listed in Table 4-4, additional input data were required for such calculations, including:

- Film cooler air purge
- Off-gas temperature at film cooler exit
- Film cooler exit pressure
- OGCT pressure
- Quencher motive fluid pressure
- Quencher motive fluid flow rate

4.2.2 *Spreadsheet Calculations*

The air inleakage and true gas temperature in the CEF vapor space were calculated iteratively by matching; (1) calculated off-gas flow at the film cooler exit with the quencher suction and (2) calculated off-gas temperature at the film cooler exit with the measured data (T15). Specifically, the calculations proceeded in the following order:

1) *Off-Gas Header ΔP* - In order to calculate the quencher suction, the ΔP across the off-gas header between the quencher inlet and where the film cooler exit pressure is measured was first calculated using:[26]

$$\Delta P = 0.000000280\, K\, W\text{^}2/(D\text{^}4\, \rho)(27.7073) \qquad (14)$$

where ΔP is in inches of H_2O ("H_2O), W the off-gas flow rate in lb/hr, D the inside diameter of the off-gas header in ft, ρ the off-gas density in lb/ft^3, and *K* the resistance coefficient calculated as:

$$K = (12\, n_{90} + 50\, n_{RB} + L/D) f_T + 0.5804 \qquad (15)$$

where n_{90} is the number of 90° elbows, n_{RB} the number of return bends, L the total length of straight pipe in ft, and f_T the friction factor for turbulent pipe flow. The nominal 2" off-gas header has no 90° elbow, one return bend, and one 45° bend with expansion. The extent of iterative calculations involved can be seen from Eq. (14), which shows that the off-gas header ΔP depends on not only the off-gas flow rate, which includes one of the unknowns, CEF air inleakage, but the density which depends on the off-gas composition and temperature. And the off-gas temperature in turn depends directly on the temperature of the off-gas exiting the melter, which is the other unknown, the true vapor space gas temperature.

Table 4-4. Input and Output of CEF Phase 1 Off-Gas Calculations.

Target vapor space temp (°C)	700	600	500	400	350	<300
- Actual vapor space temp (°C)	693	596	507	409	346	287
Vapor space pressure ("H_2O)	-5.04	-5.23	-4.74	-3.50	-3.14	-0.50
CEF-to-DWPF glass pour ratio	0.0174	0.0164	0.0161	0.0116	0.0107	0.0105
Mass flows to vapor space (lb/hr):						
calcine gases:						
- CO_2	0.4637	0.4358	0.4295	0.3084	0.2857	0.2797
- H_2O	0.4178	0.3926	0.3870	0.2778	0.2574	0.2520
- CO	0.0331	0.0311	0.0307	0.0220	0.0204	0.0200
- N_2	0.0444	0.0417	0.0411	0.0295	0.0273	0.0267
- H_2	0.0085	0.0079	0.0078	0.0056	0.0052	0.0051
- SO_2	9.4E-06	8.8E-06	8.7E-06	6.2E-06	5.8E-06	5.6E-06
- NH_3	3.6E-06	3.4E-06	3.3E-06	2.4E-06	2.2E-06	2.1E-06
- CH_4	3.0E-06	2.8E-06	2.8E-06	2.0E-06	1.9E-06	1.8E-06
volatiles:						
- free water	6.7409	6.3347	6.2439	4.4825	4.1528	4.0653
- HCOOH	0.0864	0.0812	0.0800	0.0575	0.0532	0.0521
air purges (scfm):						
- camera air purge	9.14	9.19	9.22	9.10	10.56	14.43
- vapor space air purge	0.62	0.57	8.22	18.97	22.46	28.00
Off-Gas Calculations:						
Film cooler air purge (scfm)	14.56	14.77	15.05	7.81	5.63	5.64
Film cooler exit pressure ("H_2O)	-5.52	-5.68	-5.55	-4.61	-4.32	-2.01
Off-gas header ΔP ("H_2O)	0.44	0.41	0.64	0.77	0.81	1.00
Quencher motive pressure (psig)	116.4	115.4	143.0	151.0	151.0	151.0
OGCT pressure ("H_2O)	-1.55	-1.5	-1.4	-1.2	-1.3	-1
Quencher draft ("H_2O)	4.41	4.59	4.79	4.18	3.83	2.02
Quencher design suction (acfm)	71.27	65.94	80.47	87.79	88.30	95.56
- Actual quencher suction (acfm)	71.27	65.95	80.47	87.79	88.31	95.56
Measured off-gas temp (°C)	324.8	271.6	257.6	253.1	235.4	210.2
- Calculated off-gas temp (°C)	324.8	271.6	257.6	253.1	235.4	210.2
Calculated CEF parameters:						
- Air inleakage (scfm)	7.59	8.07	9.04	10.88	10.28	8.23
- Vapor space gas temp (°C)	520	436	371	295	261	230
Off-gas concentrations:						
CO_2-MS (vol%)	0.328	0.324	0.219	0.164	0.165	0.141
CO_2-calc	0.288	0.269	0.208	0.138	0.127	0.114
CO-FTIR (ppmv)	81	91	38	26	29	21
CO-calc	291	253	278	132	110	90
H_2-GC (ppmv)	32	117	95	71	74	64
H_2-calc	160	225	215	282	311	285
Ar-MS	1.056	1.051	1.016	1.002	0.952	0.943
Ar-calc (vol%)	0.998	0.999	0.987	0.980	0.943	0.942
Carbon balance (%):	-5.7	-11.5	5.8	-9.2	-17.8	-14.0

2) *Quencher Suction* - Once the off-gas header ΔP was calculated, it was subtracted from the measured film cooler exit pressure (P3) to calculate the quencher inlet pressure and finally the quencher draft by subtracting the quencher inlet pressure from the measured OGCT pressure, as shown in Table 4-4. The quencher draft was then used to determine the suction from the vendor-provided performance curve of the 3" scrubber model FIG. 7007 by Schutte & Keorting.[27] Since the suction capacity estimated from the performance curve is for air at 20°C, the actual suction was calculated by taking into account the density difference between air and the CEF off-gas:

$$Q = Q_{air}\sqrt{\rho_{air}/\rho} \quad (16)$$

where Q is the suction capacity in acfm, and ρ the density in lb/ft^3.

3) *Estimation of Unknowns* - The CEF air inleakage rate was varied along with the true vapor space gas temperature, until the calculated off-gas flow and temperature at the film cooler exit matched the quencher suction (*Q*) and the measured temperature (*T15*) simultaneously, as shown in Table 4-4. It is noted that every iteration cycle began by updating the vapor space combustion kinetic parameters and all relevant component and stream properties such as heat capacity of the CEF exhaust and downstream flows.

4) *Calculation of Off-Gas Composition* – The concentrations of all major off-gas components, including N_2 and O_2 although not shown in Table 4-4, were calculated on a dry basis in order to facilitate comparison with the measured data using MS, GC, and FTIR. Since the measured concentrations exceeded the calibration ranges of the instruments occasionally, the data had to be scrubbed in order to determine which of the redundant measurements made using multiple instruments was the most reliable for a given species. For example, MS data were determined to be the most accurate for CO_2, while it was FTIR for CO data, as shown in Table 4-4. The carbon balance for each steady state was calculated by comparing the sum of measured CO and CO_2 to that calculated by multiplying the measured TOC concentration in the feed by the time-averaged feed rate.

4.2.3 *Spreadsheet Output*

The key results of mass and energy balance calculations shown in Table 4-4 are discussed next.

4.2.3.1 CEF Air Inleakage

The calculated air inleakage rates during Phase 1 are plotted in Figure 4-1 against the square root of the differential pressure between the CEF vapor space and the ambient. Also plotted in Figure 4-1 are the corresponding feed rates at those air inleakage rates. Contrary to the normal trend of decreasing air inleakage with decreasing differential pressure, the calculated air inleakage rates are shown to increase as the CEF pressure was reduced from -5.0 to -3.1" H_2O. It was not until the differential pressure driving force became the smallest during Phase 1 at the CEF pressure of -0.5" H_2O when the trend was finally reversed back to normal; however, the air inleakage rate at that point was still close to the initial value at -5" H_2O, instead of approaching zero.

This unexpected trend in the air inleakage-vs.-differential pressure may be attributed to the design changes made to the pour tube assembly in 2013. In the earlier design, the squared top of the pour tube was closed except for a small hole cut on the side to prevent potential glass siphoning, and it is likely that this vent hole was buried under the cold cap as the feed rate was maintained high at up to 350 g/min during the 2010 CEF run. Even if the vent hole had remained open, there would have been little chance for air inleakage from below through the pour tube, since the pour rate remained high enough to fill the pour tube with flowing glass. As a result, the calculated air

inleakage rates during the 2010 CEF run monotonically decreased as the differential pressure was reduced. By contrast, the squared top of the pour tube was cut completely open to the vapor space in the 2013 design to allow insertion of an auxiliary heater into the annular space between the pour tube and the rectangular outer pipe which was in contact with the melt in order to facilitate glass pouring during low vapor space temperature runs. Furthermore, the top of the pour tube was not only open but made taller like a chimney so there was little chance of the cold cap materials spilling over into the pour tube especially when the feed rates during Phase 1 were lower by a factor of 3 to 7 than those during the 2010 run. Therefore, as the feed rate was gradually reduced with each drop in the target vapor space temperature, the already-low glass pour rate was reduced even further, which likely opened up a passage for air infiltration inside the pour tube extending from under the CEF assembly to the vapor space. In fact, air infiltration through the pour tube was so high during the lowest vapor space temperature run at 287°C and therefore the lowest feed rate of 53.7 g/min that at a mere vacuum of -0.5" H_2O the estimated air inleakage was still in the same range as those at near -5" H_2O. Again, the accurate estimation of air inleakage was crucial to the successful completion of the Phase 1 scope.

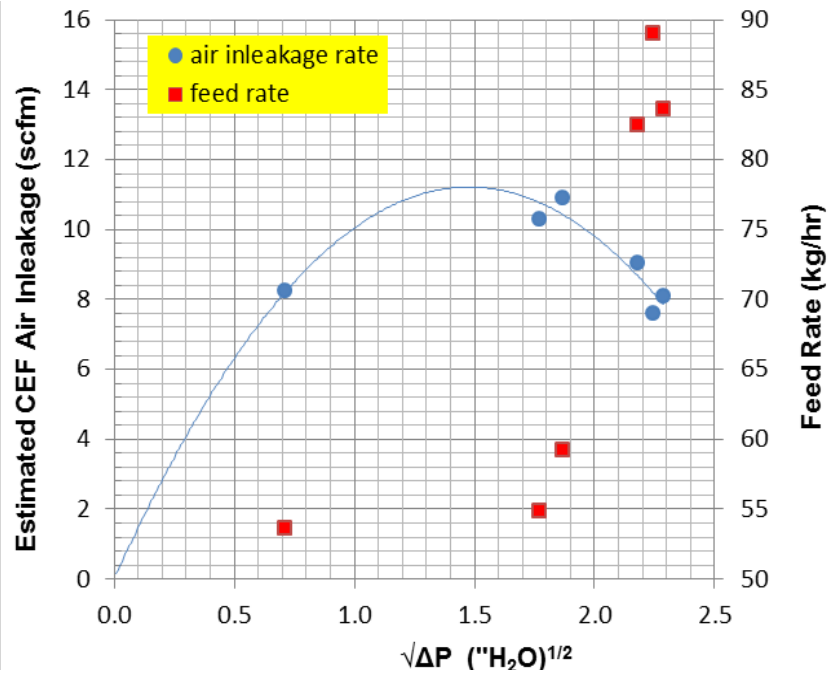

Figure 4-1. Calculated CEF Air Inleakage and Measured Feed Rates.

4.2.3.2 Vapor Space Gas Temperature

The calculated gas temperatures in the CEF vapor space are plotted in Figure 4-2 against the measured data during Phase 1. As expected, the measured temperatures were higher than the calculated gas temperatures due to infrared radiation incident on the thermowell, while gases are mostly transparent to such radiation. For example, at the measured vapor space temperature of 693°C, the calculated gas temperature was 520°C for a ΔT of 173°C. However, at the measured vapor space temperature of 287°C, the calculated gas temperature was only 57°C lower, which was expected since the impact of infrared radiation decreases with decreasing temperature. This trend is shown in Figure 4-3; ΔT between measured and calculated gas temperatures decreased logarithmically with decreasing temperature during Phase 1.

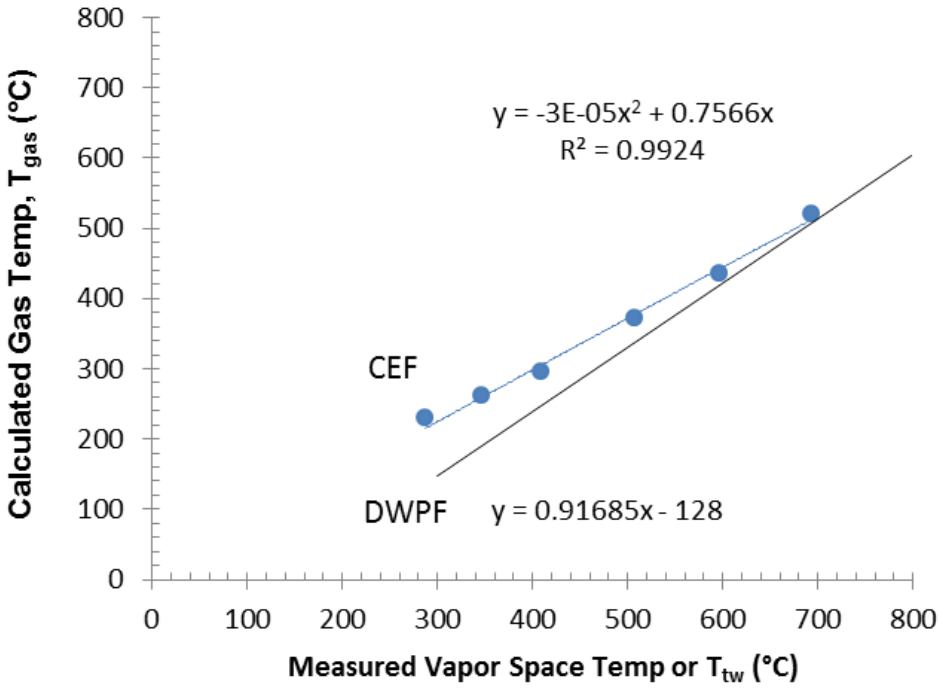

Figure 4-2. Calculated CEF Vapor Space Gas Temperatures vs. Measured Data.

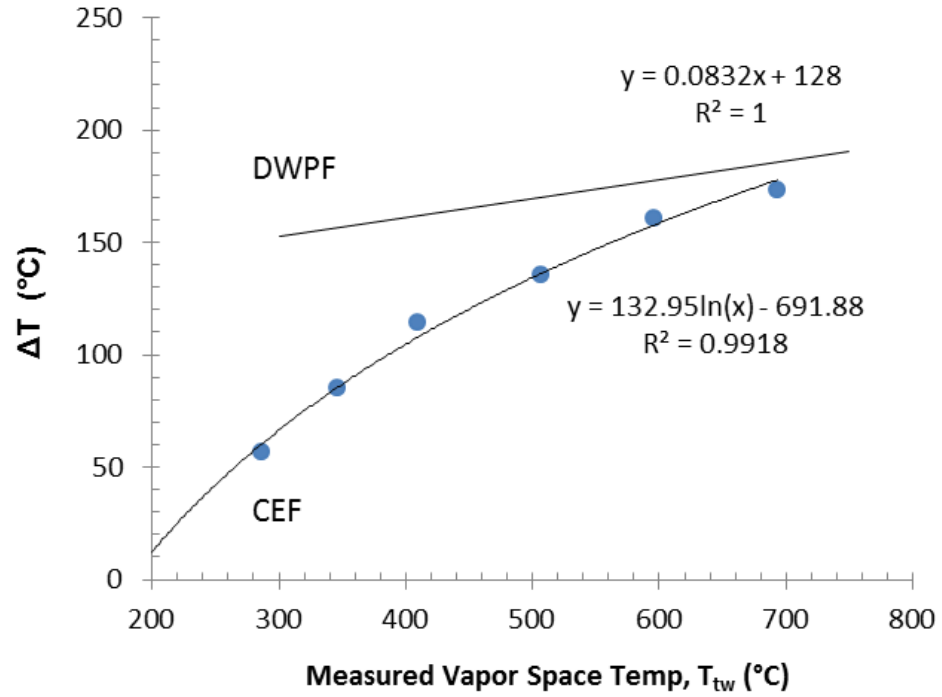

Figure 4-3. ΔT between Measured and Calculated CEF Vapor Space Gas Temperatures.

Also shown in Figure 4-2 is the correlation used to estimate the true gas temperature (T_{gas}) in the DWPF melter vapor space for the global combustion kinetic calculations:

$$T_{gas} = 0.91685\ T_{tw} - 128\ ,\ T_{tw} \leq 705°C \quad (17)$$

where T_{tw} is the measured vapor space temperature inside a thermowell, as indicated by TI4085D. Eq. (17) was derived by linearly extrapolating the calculated T_{gas} from the mass/heat balance over a narrow range of T_{tw} from 570 to 705°C during the 9th Scale-Glass Melter run (SGM-9).[7] This is precisely the reason for the DWPF melter vapor space gas temperatures continuing to decrease with decreasing TI4085D without a hint of ever slowing down like the Phase 1 data, as shown in Figure 4-2. As a result, the ΔT correlation for the DWPF melter is shown in Figure 4-3 to be also linear, which is not in accordance with the theory of radiative heat transfer; the rate of decrease in ΔT should accelerate as T_{tw} decreases, as shown by the Phase 1 data, so that ΔT approaches near zero or the measured and true gas temperatures become indistinguishable at some low T_{tw}. Therefore, the degree of under prediction of T_{gas} by Eq. (17) would increase as T_{tw} becomes lower, resulting in slower global combustion kinetics and more conservative DWPF safety basis.

It is further shown in Figure 4-2 that the calculated CEF vapor space gas temperature at the measured temperature of 693°C is essentially the same as that of SGM-9, while that at 570°C is slightly above the SGM-9 data. This means that the thermal characteristics of the 1/2 scale SGM and the 1/12 scale CEF vapor spaces are similar and, therefore, the design of the CEF vapor space is prototypic, which in turn means that the CEF thermal data are scalable to the SGM and DWPF. One immediate implication of this finding is that Eq. (17) could be replaced with the quadratic CEF temperature correlation shown in Figure 4-2 not only because of the scalability of the CEF data but because it covers a much wider temperature range, including the current TSR minimum TI4085D of 460°C (without instrument uncertainties). For example, Eq. (17) predicts T_{gas} = 294°C at T_{tw} = 460°C, while the CEF correlation predicts T_{gas} = 337°C, which is 43°C higher.

4.2.3.3 CEF Off-Gas Flammability

The calculated concentrations of H_2 and CO are compared to the measured data in Table 4-4. It appears that all calculated concentrations are considerably higher than those measured during six steady state runs, which indicates that the current DWPF model over predicted the flammability of the CEF off-gas by a wide margin, and thus setting the safety controls based on the current model predictions would seem overly conservative. However, since the key operating variables affecting off-gas flammability such as feed rate, temperature, and air purge were all varied from one steady state to the next, the instantaneous flow rates of H_2 and CO given in Table 4-4 do not properly reflect the changes in the overall combustion efficiency as a result of varying operating conditions in both the cold cap and vapor space. Therefore, the molar flow rates of H_2 and CO in the off-gas were normalized with the respective feed rate of TOC for each steady state run and the resulting H_2/TOC and CO/TOC ratios are plotted in Figure 4-4 and Figure 4-5, respectively, as a function of vapor space gas temperature, T_{gas}.

Figure 4-4 shows that both calculated and measured H_2/TOC ratios increased as the vapor space gas temperature decreased, although the rate of increase in the measured data was more gradual. This monotonic increase was expected, since the combustion kinetics slows down as temperature decreases. The margin of safety between the calculated and measured H_2/TOC ratios appears to be adequate at $T_{gas} \geq$ ~370°C; however, it becomes increasingly excessive as T_{gas} decreases below ~370°C, which is due in part to a considerable slowing down in the oxidation kinetics of H_2, as shown in Figure 4-6. For example, the first-order global combustion rate constant of H_2 decreases by a factor of 6 as T_{gas} decreased from 436 to 371°C during Phase 1.

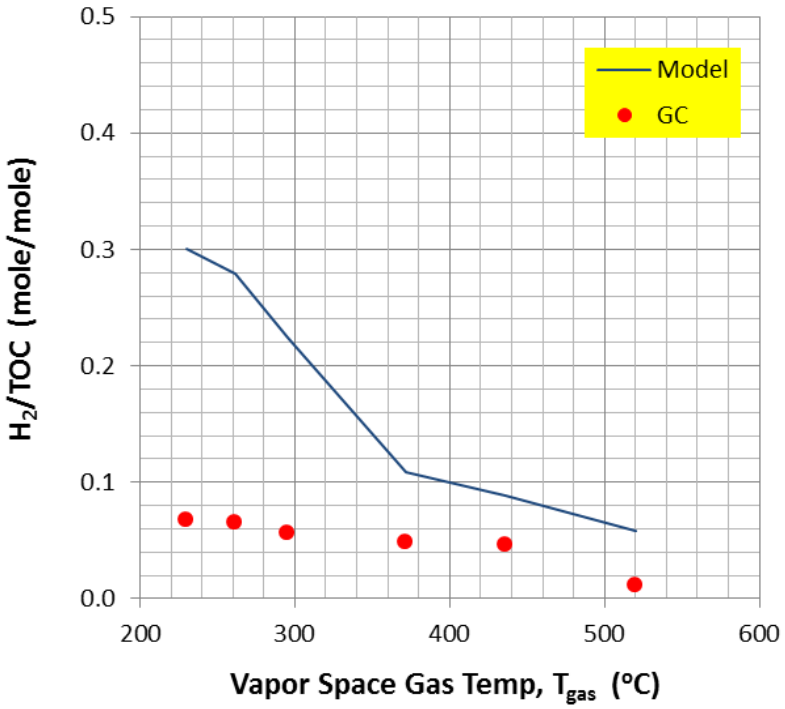

Figure 4-4. Calculated vs. Measured H_2/TOC Ratios during Phase 1.

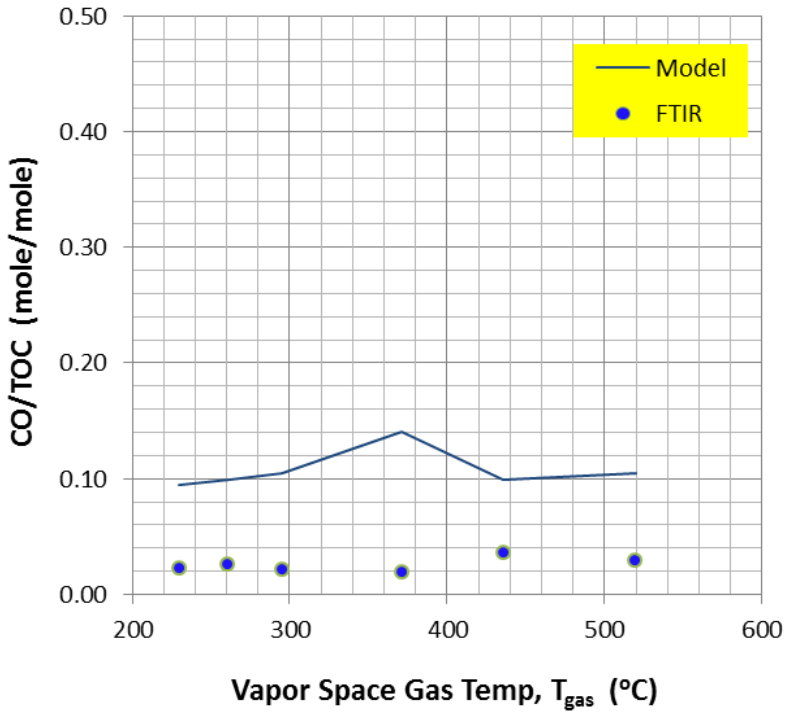

Figure 4-5. Calculated vs. Measured CO/TOC Ratios during Phase 1.

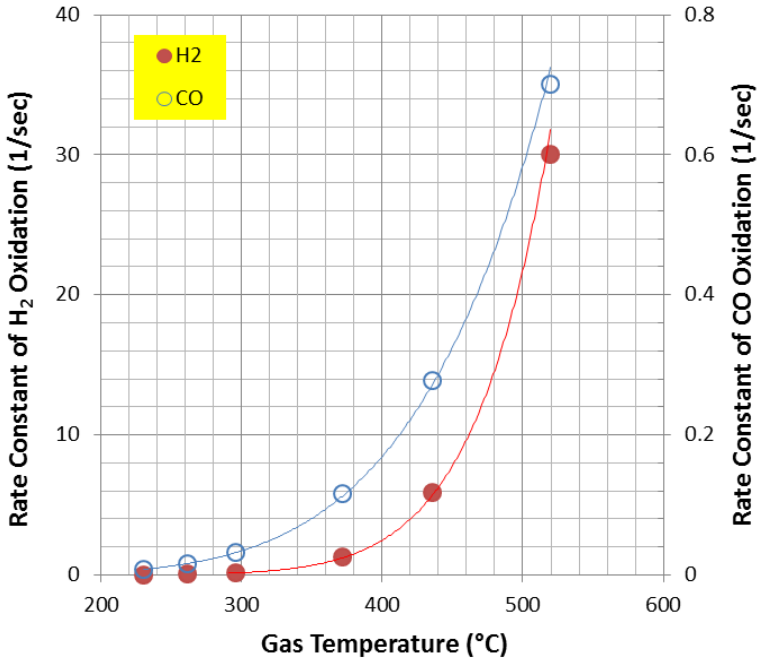

Figure 4-6. 1st Order Global Kinetics of H_2 and CO Oxidation.

When the 774-A melter was fed with a nitric-formic acid flowsheet feed that contained neither antifoam nor free formic acid, both the calculated and measured H_2/HCOOH ratios also increased sharply at $T_{gas} \leq$ ~350°C before slowing down at ~250°C,[7] which agrees well with the predicted H_2/TOC profile shown in Figure 4-4. However, one key difference between the two runs is that at $T_{gas} \leq$ ~350°C the current DWPF model over predicted the Phase 1 data by a wide margin, while the original model bounded the 774-A melter data with no such excessive conservatism. Since the main difference between the original and current DWPF models is that the antifoam and formic acid decomposition schemes were not included in the former but added to the latter recently, a sensitivity analysis was performed to determine the likely cause for the excessive conservatism in the current model vs. the Phase 1 data.

Shown in Figure 4-7 and Figure 4-8 are the calculated H_2/TOC and CO/TOC ratios, respectively, based on two bounding scenarios of formic acid decomposition: 100% dehydration (green) and 100% decarboxylation (blue). Since it is the decarboxylation pathway (Eq. 8) that produces H_2, the predicted H_2/TOC ratios at 100% dehydration are shown to be lower than those at 100% decarboxylation at all temperatures. However, the difference between the two bounding scenarios is very small at $T_{gas} \leq$ ~300°C and both predictions are higher than the Phase 1 data by a factor of 3 or higher, as shown in Figure 4-7. This suggests that at these low temperatures the overall formic acid decomposition rate is low enough that the large over prediction of the Phase 1 data by the current model is more than likely due to the conservatism in the way the decomposition of antifoam and subsequent reactions of its decomposition products in the cold cap are modeled.

Figure 4-7 also shows that the predicted H_2/TOC ratios for the two bounding scenarios begin to diverge at $T_{gas} >$ 300°C. At $T_{gas} >$ ~370°C, the predicted H_2/TOC ratios at 100% dehydration are lower than the measured data, while those at 100% decarboxylation remain considerably higher, which suggests that formic acid decomposed actively via the decarboxylation pathway during Phase 1. The predicted H_2/TOC ratios shown in Figure 4-4 were calculated assuming that 40 to 60% of the total formic acid decomposed at $T_{gas} >$ ~370°C were by the decarboxylation pathway.

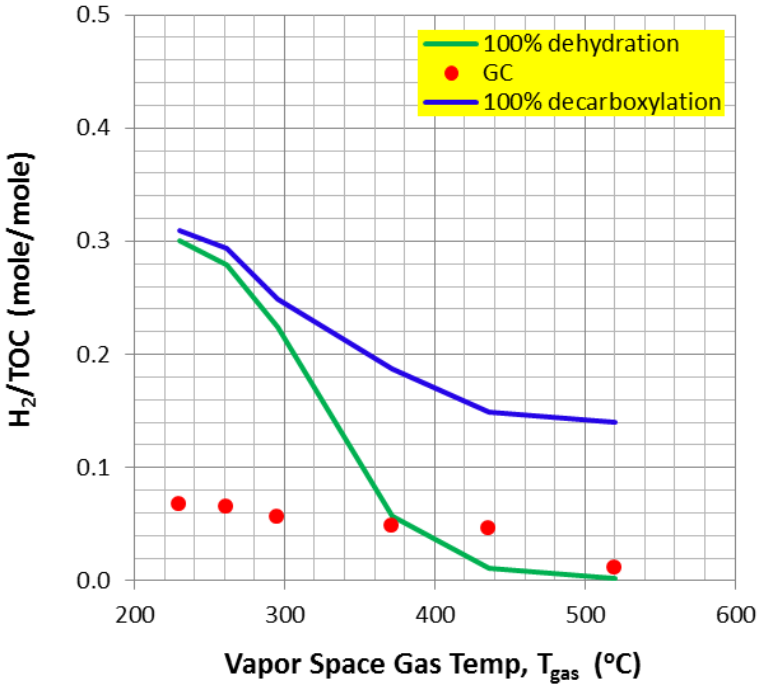

Figure 4-7. Impact of Formic Acid Decomposition on H_2/TOC Ratio during Phase 1.

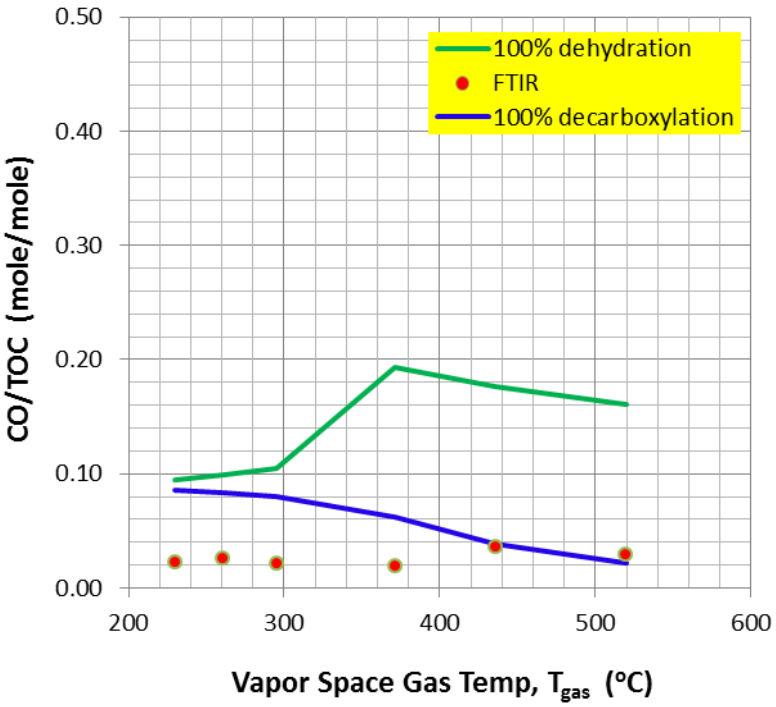

Figure 4-8. Impact of Formic Acid Decomposition on CO/TOC Ratio during Phase 1.

Unlike the H_2/TOC profiles discussed so far, both the calculated and measured CO/TOC profiles during Phase 1 are shown in Figure 4-5 to be more or less flat at all temperatures. However, the calculated CO/TOC ratios were always higher than those measured, as was the case with H_2. It is also noted that at T_{gas} < 400°C both the calculated and measured CO/TOC ratios were lower than their H_2 counterparts by a factor of ~3; however, as T_{gas} increased above 400°C, they became equal or even higher than their H_2 counterparts. Furthermore, it appears counterintuitive from the combustion kinetics standpoint that the measured concentrations of CO at T_{gas} > 400°C were the same as or even slightly higher than those measured at T_{gas} < 400°C. However, these trends were correctly predicted by the model; the increased production of CO at higher temperatures as a result of a sharp increase in the overall formic acid decomposition rate was enough to compensate for the increased consumption of CO due to the increased global combustion kinetics of CO.

Since it is the dehydration pathway that produces CO, the calculated CO/TOC ratios at 100% dehydration are shown in Figure 4-8 to be always higher than those at 100% decarboxylation. As was the case for the H_2/TOC ratios, the difference between the calculated CO/TOC ratios based on these two bounding formic acid decomposition scenarios is small at $T_{gas} \leq$ ~300°C and begins to diverge at T_{gas} > 300°C. The calculated CO/TOC ratios at 100% decarboxylation continue to decrease and eventually become close to the measured data at $T_{gas} \geq$ ~435°C, while those at 100% dehydration remain considerably higher. These observations again suggest that the antifoam decomposition scheme used in the current model is responsible for the large conservatism in the predicted CO/TOC ratios at $T_{gas} \leq$ ~300°C, and formic acid actively decomposed by the decarboxylation pathway at T_{gas} > ~300°C during Phase 1. From the overall off-gas flammability standpoint, however, the impact of CO on the DWPF safety bases is small, since its lower flammability limit (LFL) in air is more than 4X higher than that of H_2, and the measured concentration of CO is typically lower than that of H_2 at T_{gas} < ~500°C, as shown in Table 4-4.

4.3 Further Analysis of CEF Phase 1 Data

Some of the Phase 1 data not yet discussed is analyzed next in light of model validation results.

4.3.1 Criteria for Steady State Operation

On a macroscopic level, a melter operation at a given feed rate is deemed steady state when the variations in the glass and off-gas flows along with the temperature and pressure profiles remain within specified tolerances. The steady state criteria used for the Phase 1 CEF run further included a requirement on the component mass flows; the off-gas readings (H_2, CO_2, NO_x) should fluctuate less than ±10-15%. In addition, an overall carbon balance was also performed on each of the six steady state data sets to determine how close the actual operating conditions were to a steady state, and the results of carbon balance shown in Table 4-4 were calculated as:

$$\frac{(calculated\ carbon\ flow\ from\ feed\ rate - measured\ carbon\ flow\ as\ CO/CO2)*100}{measured\ carbon\ flow\ as\ CO/CO_2} \quad (18)$$

Specifically, the first term "carbon flow from feed rate" was calculated by multiplying the average feed rate by the measured TOC concentration, while the term "carbon flow as CO/CO_2" was calculated by multiplying the quencher suction by the measured CO/CO_2 concentrations. The CO_2 data shown in Table 4-4 reflect the MS readings adjusted down by an estimated 5% offset. It is shown that the carbon balance results for the runs at 700, 500, and 400°C target vapor space temperatures are all within ±10%, which indicates that the prevailing operating conditions during those runs represented the steady state reasonably well. However, it does not appear to be the case for the 600, 350 and 300°C runs, since their carbon balances were outside the ±10% tolerance

particularly for the 350 and 300°C runs. In fact, the carbon balance of -11.5% for the 600°C run may still be considered reasonable considering the uncertainties in the feed data such as TOC as well as the operational difficulty in maintaining steady calcine gas flow under the dynamic cold cap conditions.

It is also noted that the Phase 1 carbon balances were all negative except for the 500°C run, which means that more carbon exited the system than came in with the feed. Obviously, this condition cannot be sustained indefinitely since there is a finite inventory of carbon in the cold cap. This temporal net outflow of carbon is possible under three different scenarios: (1) After the CEF had been overfed for some time, the total carbon flow exiting the cold cap would include carbon species produced from a rather thick layer of decomposing salts, (2) the estimated off-gas flow, including air inleakage, was too high, or (3) the CO_2 were measured too high. In fact, the CO_2 readings by MS, which were taken as the most accurate in this study, fell between the FTIR and GC data; had the FTIR data been taken instead, the resulting carbon balance would have been mostly positive, although the absolute scale of deviations would have been greater. Nevertheless, Scenario (3) was discarded since its plausibility depends solely on the accuracy of instruments used, and thus its impact would have been the same in all runs. Scenario (2) was also discarded since all air purges were measured using calibrated flow meters and the estimated air inleakage rates did not make up a significant portion of the quencher suction during the 350 and 300°C runs.

That leaves overfeeding as the only plausible scenario for not achieving a steady state during the 350 and 300°C runs, and there appears to be two experimental indicators that may be used as a sign of overfeeding. The first is by way of a direct viewing of the cold cap using a remote camera, as was done during Phase 1. Figure 4-9 shows the still images of the cold cap videotaped during the 500 and 350°C runs which represented the best and worst carbon balances, respectively. Although these images were taken while the CEF was running under non-bubbled conditions, a minimum argon flow of ~0.005 scfm was still maintained to each bubbler in order to prevent the line from plugging. As a result, argon exited the melt pool through a vent hole formed right at the bubbler; one of the two bubblers is visible in the upper middle-left of each image. Furthermore, these vent holes not only moved around the bubblers but oscillated in size between the maximum (upper images) and the minimum (lower images). The lower left image shows a shrinking vent hole as the fresh feed spread out (dark region), whereas no vent hole is visible in the lower right image, and the entire viewing area is completely dark, which clearly shows overfeeding.

Another distinct sign of overfeeding during the 350°C run is that a thin, bright arc clearly visible all along the wall in the left-hand images is only partially visible in the right-hand images. This arc is formed as a result of feed material spreading out and melting at the wall since the bottom 6” of the Inconel wall is heated above 1,100°C so at the 9” mark where the cold cap is located the wall temperature should be still close to 1,100°C. Clearly, the feed rate during the 350°C run was high enough even to overwhelm the melting at the wall.

Figure 4-9. Cold Cap Views during Non-Bubbled Phase 1 Runs.

Another indicator that may be used to help achieve steady state would be by monitoring the melt temperatures. Figure 4-10 shows the upper (T13) and lower (T14) melt temperature profiles during Phase 1, both of which were measured a few inches from the center. Vertically, the lower melt temperature is measured at ~1" above the bottom whose temperature is maintained at above 1,100°C, while the upper melt temperature is measured at ~2" below the cold cap which acts as a heat sink. Hence, the normal temperature distribution is T13 < T14 under non-bubbled conditions with the difference between them typically being less than 80°C. It is shown in Figure 4-10 that the normal temperature distribution was maintained throughout the 500°C run whose carbon balance was not only the best (along with the 700°C run which also had the normal temperature profile) but positive. For the 350°C run, however, the temperature profile was inverted, i.e., T13 > T14. The cause for the inversion is not known, although it might have been triggered by overfeeding, as the growing cold cap extended further into the melt and eventually some portion of it got swept away by the downward melt current in the middle, thus lowering T14, as shown in Figure 4-10.

In case of severe overfeeding, the cold cap grows so thick that it would penetrate into the upper melt pool, causing T13 to drop by a few hundred degrees, as happened during the melter turnover and the feed ramp-up following the steady state runs in Phase 1. In both cases, the feed rate was maintained or ramped up intentionally at a very high rate, which certainly would have resulted in flooding of the cold cap under the circumstances.

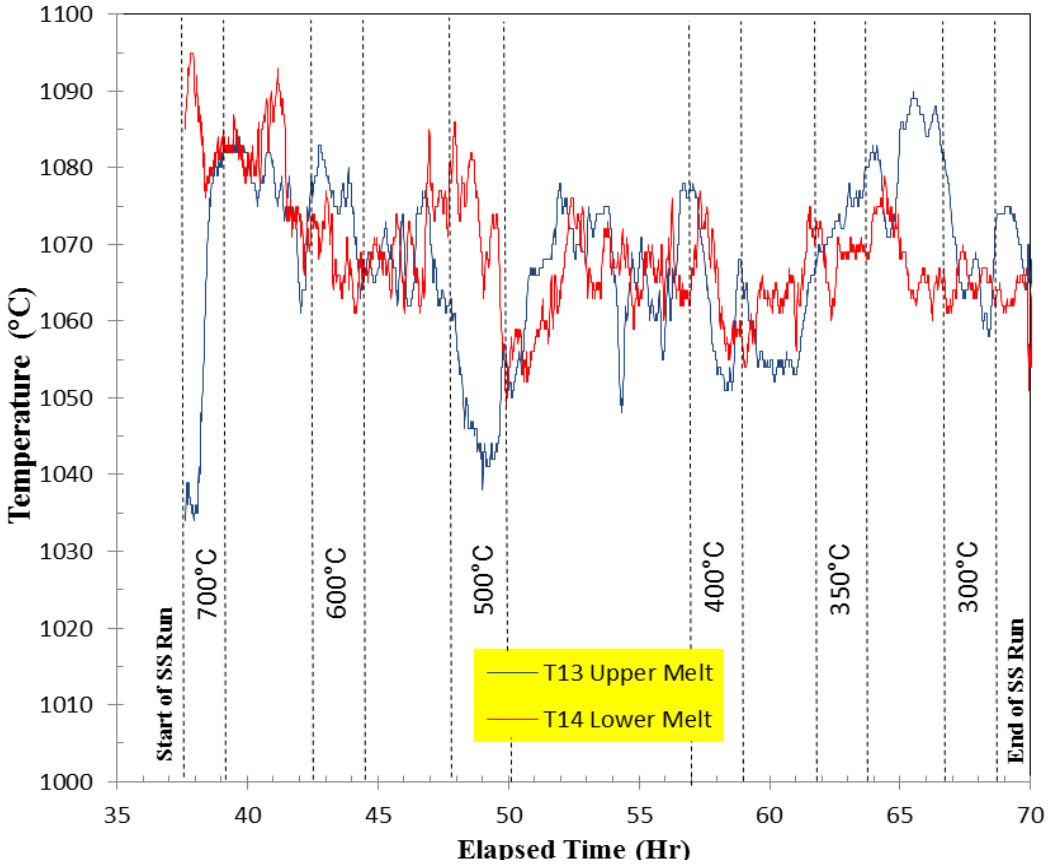

Figure 4-10. Melt Temperature Profiles during Phase 1 CEF Run.

The inversion of the melt temperature profile was also seen during the 600°C run, whose carbon balance was also outside the ±10% tolerance. A large temperature inversion also occurred in the beginning of the 300°C run, even though it was restored back to the normal distribution only toward the end. In summary, it appears that maintaining the normal melt temperature profile of T13 < T14 with a difference of 20°C or more between them is important to maintaining a steady state; the inverted melt temperature profile or the two melt temperatures being close to each other appears to be undesirable under non-bubbled conditions.

4.3.2 *Redox Profile of CEF Phase 1 Glass*

The redox profile of glass samples pulled from the CEF during Phase 1 is shown in Figure 4-11 along with that of the feed rate. The CEF was initially filled with the glass cullet from the 2010 CEF run whose measured redox was zero. As a result, the redox is shown to steadily increase during the first 20 or so hours of feeding and eventually leveled off at near 0.18 after enough feed was processed for one melter turnover. It was expected that this plateaued redox value would be lower than the measured redox of 0.26 in a sealed crucible, as the startup glass would not have been completely flushed out in just one melter turnover and had the melt pool not been agitated using the argon bubblers. However, the bubblers were turned on throughout the turnover at more than 2X the DWPF bubbling flux (defined as scfm Ar/ft^2 melt surface) so the redox was expected to be closer to or even somewhat higher than the sealed crucible data, since bubbling is known to increase the redox of DWPF glass by 0.1.[28] As discussed earlier, air infiltration through the pour tube would not have occurred at the high feed rates during the turnover, which means that a brief

contact with air during the "free fall" of fast-flowing glass stream was not likely to have exerted enough oxidizing potential to counterbalance the reducing effects by the bubbling. Therefore, it is likely that argon bubbling had less reducing effects on the CEF glass than on the DWPF glass.

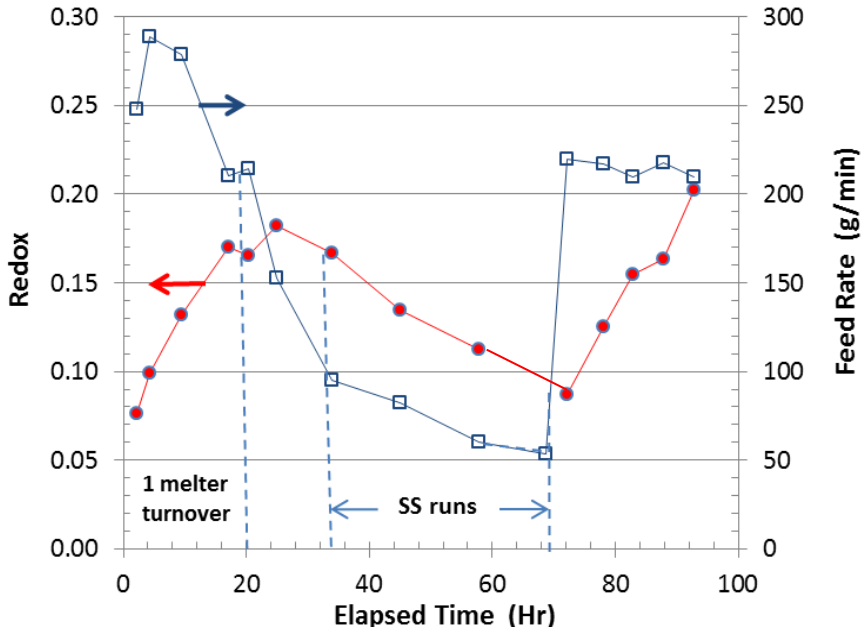

Figure 4-11. Glass Redox and Feed Rate Profiles during Phase 1.

After redox plateaued, the bubblers were turned off and preparations were underway for the steady state tests which began at 37th hour and lasted through 70th hour with steadily decreasing feed rate, as shown in Figure 4-11. It is seen that redox also decreased steadily to 0.08 at the end of the steady state runs. One possible explanation for this steady decline in redox with decreasing feed rate is that as the pour rate continued to decrease eventually to a fine thread or intermittently zero near the end, the effective cross-sectional area for air infiltration inside the pour tube continued to increase, resulting in a prolonged contact between glass and air before its free fall. Supporting evidence for this comes from the estimated air inleakage rates discussed earlier; it kept increasing with decreasing feed rate even as the differential pressure driving force was reduced, and the estimated air inleakage at the mere vacuum of -0.5" H_2O still remained as high as those at near -5" H_2O.

The steady decline in redox during the steady state runs may also be regarded as the manifestation of non-bubbled operation; the melt pool was merely recovering from the reducing conditions brought on by the bubbling during the turnover to its true redox state in the absence of bubbling. One problem with this view is that the measured redox continued to move further away from the sealed crucible data. In order for this view to hold, the contact between glass and air that occurred both inside and outside (free fall) the pour tube during the latter part of the steady state runs should have been significant enough to cause a redox decline of 0.18 (from 0.26 to 0.08), since the melter turnover would have been completed by 70th hour. By comparison, the redox of the glass samples pulled from the 774-A melter averaged 0.1 despite the fact that the feed was more oxidizing than the Phase 1 feed, and the degree of contact of the cold cap and glass with air remained very high throughout due to a significant melter air inleakage coupled with a very low cold cap coverage of only around 20% compared to >90% during Phase 1.[7]

Beginning at 70th hour, the feed rate was ramped up quickly from near 50 to 220 g/min with the bubblers turned on, and the redox is shown to bounce back more quickly than it decreased after the bubblers were turned off. Again, at such high feed rates, the contact between glass and air would have been limited to the free fall so the redox should have recovered to the initial peak value of 0.18 rather quickly. However, it took almost 20 hours to restore the initial redox, which suggests that the increase in redox after 70th hour was in part due to bubbling.

Based on the discussions made so far, it is concluded that the known impact of bubbling vs. non-bubbling on redox could explain the measured profile but only qualitatively, and the impact of air inleakage on redox has to be significant in the current CEF design in order to explain the large discrepancies that exist between the redox of pulled glass and the sealed crucible data.

5.0 Implications to DWPF

The main goal of this study was to confirm whether the CEF platform selected for the nitric-glycolic acid flowsheet melter demonstration is capable of producing scalable melter off-gas data necessary for the revision of the DWPF melter off-gas flammability model; the revised model will be used to define the new safety controls and optimize the operating parameters for the nitric-glycolic flowsheet. Figure 4-4 and Figure 4-5 show that the current DWPF model correctly predicts the qualitative trends of the measured H_2 and CO data in the CEF off-gas and further bounds them by over predicting with an adequate margin of safety; (1) the TOC-to-H_2 conversion for T_{gas} > ~350°C and (2) TOC-to-CO conversions for all T_{gas}; the seemingly-excessive over prediction of TOC-to-H_2 conversion (or H_2/TOC ratio) for T_{gas} < ~350°C is attributed to the conservative antifoam decomposition scheme added to the current model and thus is considered a modeling issue not a design issue. Therefore, it is concluded that the CEF design is prototypic from the melter off-gas flammability standpoint, and the existing DWPF safety controls set using the current model are conservative.

Specifically, the current DWPF model predicted that at most 0.3 mole of H_2 would be produced per mole of TOC fed during Phase 1 under the "cold vapor space" conditions, whereas the highest measured TOC-to-H_2 conversion was less than 0.1 mole of H_2 per mole of TOC fed. Considering that the 774-A melter run with a more oxidizing feed that contained neither antifoam nor free formic acid produced the H_2/TOC ratios comparable to those of Phase 1 at T_{gas} < ~350°C,[7] it is apparent that the antifoam decomposition scheme via Eq. (1) and subsequent cold cap reactions added to the current DWPF model result in too high H_2 concentrations in the calcine gas input into the vapor space combustion model. This finding was further substantiated by the results of the sensitivity analysis of formic acid decomposition performed during this study. Therefore, improving the antifoam decomposition scheme used in the current model should be one of the main focuses of the next model revision.

It is also noted that the current model over predicted not only the H_2/TOC ratio for T_{gas} < ~350°C but the redox of the CEF Phase 1 glass by a wide margin; 0.45 vs. the average redox of 0.26 in sealed crucible tests. However, the over prediction of both off-gas flammability and redox is not consistent with the overall oxygen balance, since for a given inventory of O_2 in the feed a more oxidizing glass means less O_2 available for oxidation of flammable gases, thus more flammable calcine gas or vice versa. This suggests that there was a shortage of O_2 in the modeling space, which could have been caused by the current antifoam decomposition scheme which is set up to consume too much O_2.

In order to help resolve these issues with the current model, the data from the two tests completed recently will be analyzed in detail in order to extract further insight into the chemistry of antifoam decomposition. The first test was run in a temperature-programmed furnace with both normal and spiked feeds with fresh antifoam under inert and slightly oxidizing vapor space conditions. Both the nitric-formic and nitric-glycolic acid flowsheet feeds were used in the furnace test. The data to be analyzed include the profiles of both organic and inorganic gas species as a function of furnace temperature as well as redox of the remaining glass. The Phase 2 CEF tests were run with the baseline nitric-glycolic acid flowsheet feeds that contained the "processed antifoam" and those spiked with fresh antifoam in order to study the effects of antifoam concentration as well as its processing history on its decomposition chemistry under the actual melter conditions.

6.0 Conclusions

Based on the results of the CEF Phase 1 data analysis discussed so far, the following conclusions are drawn:

1. The CEF design is prototypic in terms of producing scalable off-gas data to support the revision of the DWPF melter off-gas flammability model.

2. The over prediction of H_2 concentration in the CEF off-gas at T_{gas} < ~350°C is attributed to the conservatism in the way the antifoam decomposition and subsequent reactions of its degradation products in the cold cap are handled in the current DWPF model.

3. Formic acid vapor decomposed actively by the decarboxylation pathway to produce H_2 and CO_2 during Phase 1, which was the main reason for the moderately conservative predictions by the current model at T_{gas} > ~350°C.

4. The measured-vs.-true gas temperature correlation derived for the CEF vapor space closely agrees with the original data used to develop the current DWPF correlation, Eq. (17), which means that the thermal characteristics of the CEF vapor space are prototypic of the DWPF melter.

5. A similar heat/mass balance approach taken in this study can be used on the DWPF data to confirm the adequacy of the CEF temperature correlation shown in Figure 4-2 and, if necessary, revise it before incorporating it into the DWPF melter off-gas flammability model in lieu of Eq. (17).

7.0 References

1. Wagnon, T. J., "Defense Waste Processing Facility Alternate Reductant Systems Engineering Evaluation," ***G-AES-S-00003***, ***Rev. 0***, Savannah River Remediation, Aiken, SC, August 3, 2011.

2. Choi, A. S., "Melter Off-Gas Flammability Assessment for DWPF Alternate Reductant Flowsheet Options," ***SRNL-STI-2011-00321***, ***Rev. 0***, Savannah River National Laboratory, Aiken, SC, July 2011.

3. Choi, A. S., and Lee, S. Y., "Impact of Melter Internal Design on Off-Gas Flammability," ***SRNL-STI-2012-00121***, ***Rev. 0***, Savannah River National Laboratory, Aiken, SC, May 2012.

4. Choi, A. S., "DWPF MOG Flammability Assessment," ***X-CLC-S-00164***, ***Rev. 4***, August 12, 2010.

5. Abramowitz1, H., Calloway, B., Mecholsky N., D'Angelo1, N., Windham, J., and Coleman, J., "Analysis of Bubbled vs. Non-Bubbled DWPF Operating Data," A Joint Report by Savannah River Remediation (Aiken, SC), Vitreous State Laboratory of The Catholic University of America (Washington, D.C.), and Savannah River National Laboratory (Aiken, SC), June 6, 2013.

6. Choi, A. S., "DWPF MOG Flammability Assessment (Sludge Batch 8)," ***X-CLC-S-00164***, ***Rev. 8***, March 8, 2013.

7. Choi, A. S., "Validation of DWPF Melter Off-Gas Combustion Model," ***WSRC-TR-2000-00100***, June 23, 2000.

8. Choi, A. S., "Validation of DWPF MOG Dynamics Model - Phase I (U)," ***WSRC-TR-96-0307***, January 7, 1997.

9. Material Safety Data Sheet: Antifoam 747, ***MSDS 33655, Rev. 1***, Taylor Chemical Company, Inc., January 9, 2007.

10. White, T. L., Wiedenman, B. J., Lambert, D. P., Crump, S. L., Fondeur, F. F., Papathanassiu, A. E. (VSL), Kot, W. K. (VSL), and Pegg, I. L. (VSL), "Organics Characterization of DWPF Alternative Reductant Simulants, Glycolic Acid, and Antifoam 747," ***SRNL-STI-2013-00491***, ***Rev. 0***, Savannah River National Laboratory, October 1, 2013.

11. Newell, J. D., "Antifoam Partitioning during SRAT Processing," ***SRNL-L3100-2011-00171***, Savannah River National Laboratory August 24, 2011.

12. Dvornic, P. R., "High Temperature Stability of Polysiloxanes, Silicon Compounds: Silanes and Silicones," Barry Arkles, Gerald Larson, Eds., ***Gelest Catalog*: *A Survey of Properties and Chemistry***, 441-454 (2008).

13. Zamecnik, J. R., *Unpublished Results of Antifoam Degradation Study*, 2013.

14. Saito, K., Shiose, T., Takahashi, O., Hidaka, Y., Aiba, F., and Tabayashi, K., "Unimolecular Decomposition of Formic Acid in the Gas Phases - On the Ratio of the Competing Reaction Channels," ***J. Phys. Chem. A***, **109**, 5352-5357 (2005).

15. Akiya, N, and Savage, P. E., "Role of Water in Formic Acid Decomposition," ***AIChE J***., **44**, 405 (1988).

16. Matlack, K. S., Kot, W. K., D'Angelo, N., Pegg, I. L., Diener, G. A., and Joseph, I. "*Final Report-Off-Gas Data from DM10 Melter Testing of Alternate Reductant Flow-Sheets for the Defense Waste Processing Facility*," ***VSL-11R2020-4, Rev. 0***, VSL, The Catholic University of America, Washington, DC, and Energy*Solutions* Federal EPC, Inc., Columbia, MD, April 26, 2011.

17. Nelson, W. L., and Engelder, C. J., "The Thermal Decomposition of Formic Acid," ***J. Phys. Chem.***, **30** (4), 470-475 (1926).

18. Wescott, B. B., and Engelder, C. J., "The Catalytic Decomposition of Formic Acid," ***J. Phys. Chem.***, **30** (4), 476-479 (1926).

19. Lambert, D. P., "Batching Recipe: Nitric/Formic Acid Flowsheet Melter Feed," ***SRNL-L3100-2013-00021***, ***Rev. 0***, March 18, 2013.

20. Johnson, F.C., Miller, D.H., Zamecnik, J.R., and Lambert, D.P., "Alternate Reductant Cold Cap Evaluation Furnace Phase 1 Testing," ***SRNL-STI-2014-00005***, January 2014.

21. Onwudili, J. A., and Williams, P. T., "Hydrothermal reactions of sodium formate and sodium acetate as model intermediate products of the sodium hydroxide-promoted hydrothermal gasification of biomass," ***Green Chem.***,**12**, pp 2214-2224 (2010).

22. Yoshimori, T., Asano, Y., Toriumi, Y., and Shiota, T., "Investigation on the drying and decomposition of sodium oxalate," ***Talanta***, **25 (10)**, pp 603-605 (1978).

23. Freeman, E. S., "The Kinetics of the Thermal Decomposition of Sodium Nitrate and of the Reaction Between Sodium Nitrite and Oxygen," ***Journal of Physical Chemistry***, **60**, pp 1487-1493 (1956).

24. Plante, E. R., Bonnell, D. W., and Hastie, J. W., "Experimental and Theoretical Determination of Oxide Glass Vapor Pressures and Activities," ***Advances in the Fusion of Glass***, **Am. Cer. Soc.**, pp 26.1-26.18 (1988).

25. Koopman, D. C., and Zamecnik, J. R., "DWPF Simulant CPC Studies for SB8," ***SRNL-STI-2013-00106***, June 2013.

26. *Flow of Fluids through Valves, Fittings, and Pipe*, **Technical Paper No. 410**, Crane Co. (1988).

27. Schutte & Koerting, *Bulletin 7-S*, Performance Curve for Fig. 7009 3-Inch Scrubber *(*2008*).*

28. Jantzen, C. M., and Johnson, F. C., "Impacts of Antifoam Additions and Argon Bubbling on Defense Waste Processing Facility (DWPF) REDuction/OXidation (REDOX)," ***SRNL-STI-2011-00652, Rev. 0***, June 2012.

Appendix A.

Tables of Steady State Operating Conditions during CEF Phase 1 Run

Variable	Ave VS Temp	Ave Melt Temp	Melter Press	FC Exit Temp	FC Exit Press	FC Air	Camera Air	VS Air	H_2 (GC)	CO (FTIR)	CO_2 (MS)	NO (FTIR)	NO_2 (FTIR)	N_2O (FTIR)
	(°C)	(^{o}C)	("wc)	(^{o}C)	("wc)	(scfm)	(scfm)	(scfm)	(ppm)	(ppm)	(vol %)	(ppm)	(ppm)	(ppm)
average	693.3	1071.9	-5.04	324.8	-5.52	14.6	9.1	0.6	32	81	0.35	382	82	44
std dev	2.3	8.0	0.19	2.3	0.19	0.2	0.1	0.0	13	19	0.04	68	12	10
max	699.5	1083.5	-4.33	331.0	-4.76	15.2	9.5	0.6	53	164	0.50	626	122	82
min	687.5	1059.5	-5.35	321.0	-5.83	14.0	8.8	0.6	0	38	0.24	215	51	25

Variable	Ave VS Temp	Ave Melt Temp	Melter Press	FC Exit Temp	FC Exit Press	FC Air	Camera Air	VS Air	H_2 (GC)	CO (FTIR)	CO_2 (MS)	NO (FTIR)	NO_2 (FTIR)	N_2O (FTIR)
	(°C)	(^{o}C)	("wc)	(^{o}C)	("wc)	(scfm)	(scfm)	(scfm)	(ppm)	(ppm)	(vol %)	(ppm)	(ppm)	(ppm)
average	596.5	1071.2	-5.23	271.6	-5.68	14.8	9.2	0.6	117	91	0.34	376	60	45
std dev	2.3	3.9	0.18	1.9	0.18	0.3	0.1	0.0	29	25	0.04	48	8	9
max	601.0	1078.0	-4.55	277.0	-5.00	15.5	9.5	0.6	191	169	0.45	499	79	73
min	593.0	1064.5	-5.52	266.0	-5.97	13.9	8.8	0.6	75	29	0.20	113	40	18

Variable	Ave VS Temp	Ave Melt Temp	Melter Press	FC Exit Temp	FC Exit Press	FC Air	Camera Air	VS Air	H_2 (GC)	CO (FTIR)	CO_2 (MS)	NO (FTIR)	NO_2 (FTIR)	N_2O (FTIR)
	(°C)	(^{o}C)	("wc)	(^{o}C)	("wc)	(scfm)	(scfm)	(scfm)	(ppm)	(ppm)	(vol %)	(ppm)	(ppm)	(ppm)
average	507.1	1060.7	-4.74	257.6	-5.55	15.0	9.2	8.2	95	38	0.23	237	28	25
std dev	4.8	5.2	0.21	2.4	0.20	0.3	0.1	0.0	33	16	0.05	53	4	7
max	515.0	1073.5	-3.77	263.0	-4.58	15.7	9.6	8.3	169	98	0.37	413	40	45
min	496.5	1052.0	-5.08	252.0	-5.87	14.1	8.9	8.1	44	9	0.12	98	15	10

Ave VS Temp = average of upper and lower vapor space temperature readings from T11 and T12.
Ave Melt Temp = average of upper and lower melt temperature readings from T13 and T14.
Camera Air = air purges to both Canty and SRNL cameras.

Variable	Ave VS Temp	Ave Melt Temp	Melter Press	FC Exit Temp	FC Exit Press	FC Air	Camera Air	VS Air	H_2 (GC)	CO (FTIR)	CO_2 (MS)	NO (FTIR)	NO_2 (FTIR)	N_2O (FTIR)
	(°C)	(^{o}C)	("wc)	(^{o}C)	("wc)	(scfm)	(scfm)	(scfm)	(ppm)	(ppm)	(vol %)	(ppm)	(ppm)	(ppm)
average	409.5	1063.3	-3.50	253.1	-4.61	7.8	9.1	19.0	71	26	0.17	179	30	17
std dev	5.9	6.7	0.35	2.9	0.34	0.2	0.1	0.6	21	10	0.02	30	5	5
max	420.5	1074.5	-1.53	258.0	-2.61	8.4	9.5	19.7	117	56	0.25	287	47	34
min	399.5	1053.5	-4.05	248.0	-5.15	7.4	8.8	18.3	36	8	0.13	134	23	9

Variable	Ave VS Temp	Ave Melt Temp	Melter Press	FC Exit Temp	FC Exit Press	FC Air	Camera Air	VS Air	H_2 (GC)	CO (FTIR)	CO_2 (MS)	NO (FTIR)	NO_2 (FTIR)	N_2O (FTIR)
	(°C)	(^{o}C)	("wc)	(^{o}C)	("wc)	(scfm)	(scfm)	(scfm)	(ppm)	(ppm)	(vol %)	(ppm)	(ppm)	(ppm)
average	346.2	1071.1	-3.14	235.4	-4.32	5.6	10.6	22.5	74	29	0.17	153	19	21
std dev	2.5	2.4	0.64	2.2	0.57	0.1	1.2	1.0	24	11	0.02	31	2	6
max	352.0	1075.0	-0.93	240.0	-2.25	5.8	14.0	23.9	142	78	0.23	292	26	47
min	340.5	1065.5	-3.89	230.0	-5.03	5.3	9.6	21.7	38	9	0.11	98	14	9

Variable	Ave VS Temp	Ave Melt Temp	Melter Press	FC Exit Temp	FC Exit Press	FC Air	Camera Air	VS Air	H_2 (GC)	CO (FTIR)	CO_2 (MS)	NO (FTIR)	NO_2 (FTIR)	N_2O (FTIR)
	(°C)	(^{o}C)	("wc)	(^{o}C)	("wc)	(scfm)	(scfm)	(scfm)	(ppm)	(ppm)	(vol %)	(ppm)	(ppm)	(ppm)
average	286.5	1066.0	-0.50	210.2	-2.01	5.6	14.4	24.4	64	21	0.15	123	14	15
std dev	2.8	2.0	0.24	2.4	0.25	0.1	0.2	0.0	19	7	0.02	18	1	4
max	293.0	1071.0	0.76	215.0	-0.68	5.9	14.9	24.4	103	49	0.18	180	19	28
min	282.5	1061.5	-0.94	207.0	-2.41	5.4	14.0	24.4	35	8	0.12	78	11	7

Distribution:

S. L. Marra, 773-A
T. B. Brown, 773-A
S. D. Fink, 773-A
C. C. Herman, 773-A
E. N. Hoffman, 999-W
F. B. Johnson, 999-W
D. H. McGuire, 999-W
F. M. Pennebaker, 773-42A
W. R. Wilmarth, 773-A
Records Administration (EDWS)

J. M. Bricker, 704-30S
T. L. Fellinger, 766-H
E. J. Freed, 704-S
J. M. Gillam, 766-H
B. A. Hamm, 766-H
E. W. Holtzscheiter, 766-H
J. F. Iaukea, 704-27S
D. W. McImoyle, 766-H
D. K. Peeler, 999-W
J. W. Ray, 704-27S
P. J. Ryan, 704-30S
H. B. Shah, 766-H
D. C. Sherburne, 704-S
M. E. Smith, 704-30S

P. R. Jackson, DOE-SR, 703-46A
K. H. Subramanian, 241-156H